Monthly Notices
of the
ROYAL ASTRONOMICAL SOCIETY

MNRAS **475,** 3429–3452 (2018)
Advance Access publication 2018 January 17

doi:10.1093/mnras/sty026

LOFAR-Boötes: properties of high- and low-excitation radio galaxies at $0.5 < z < 2.0$

W. L. Williams,[1]★ G. Calistro Rivera,[2] P. N. Best,[3] M. J. Hardcastle,[1]
H. J. A. Röttgering,[2] K. J. Duncan,[2] F. de Gasperin,[2] M. J. Jarvis,[4,5] G. K. Miley,[2]
E. K. Mahony,[6,7] L. K. Morabito,[4] D. M. Nisbet,[3] I. Prandoni,[8] D. J. B. Smith,[1]
C. Tasse[9,10] and G. J. White[11,12]

[1]*School of Physics, Astronomy and Mathematics, University of Hertfordshire, College Lane, Hatfield AL10 9AB, UK*
[2]*Leiden Observatory, Leiden University, PO Box 9513, NL-2300 RA Leiden, the Netherlands*
[3]*SUPA, Institute for Astronomy, Royal Observatory, Blackford Hill, Edinburgh EH9 3HJ, UK*
[4]*Astrophysics, University of Oxford, Denys Wilkinson Building, Keble Road, Oxford OX1 3RH, England*
[5]*Physics and Astronomy Department, University of the Western Cape, Bellville 7535, South Africa*
[6]*Sydney Institute for Astronomy, School of Physics A28, The University of Sydney, NSW 2006, Australia*
[7]*ARC Centre of Excellence for All-Sky Astrophysics (CAASTRO) Redfern, NSW 2016 Australia*
[8]*INAF – Istituto di Radioastronomia, Via P. Gobetti 101, Bologna I-40129, Italy*
[9]*GEPI, Observatoire de Paris, CNRS, Université Paris Diderot, 5 place Jules Janssen, F-92190 Meudon, France*
[10]*Department of Physics and Electronics, Rhodes University, PO Box 94, 6140 Grahamstown, South Africa*
[11]*Department of Physical Sciences, The Open University, Walton Hall, Milton Keynes MK7 6AA, England*
[12]*RAL Space, The Rutherford Appleton Laboratory, Chilton, Didcot, Oxfordshire OX11 0NL, England*

Accepted 2017 November 24. Received 2017 November 15; in original form 2017 January 6

ABSTRACT

This paper presents a study of the redshift evolution of radio-loud active galactic nuclei (AGN) as a function of the properties of their galaxy hosts in the Boötes field. To achieve this we match low-frequency radio sources from deep 150-MHz LOFAR (LOw Frequency ARray) observations to an *I*-band-selected catalogue of galaxies, for which we have derived photometric redshifts, stellar masses, and rest-frame colours. We present spectral energy distribution (SED) fitting to determine the mid-infrared AGN contribution for the radio sources and use this information to classify them as high- versus low-excitation radio galaxies (HERGs and LERGs) or star-forming galaxies. Based on these classifications, we construct luminosity functions for the separate redshift ranges going out to $z = 2$. From the matched radio-optical catalogues, we select a sub-sample of 624 high power ($P_{150\,\mathrm{MHz}} > 10^{25}\,\mathrm{W\,Hz^{-1}}$) radio sources between $0.5 \le z < 2$. For this sample, we study the fraction of galaxies hosting HERGs and LERGs as a function of stellar mass and host galaxy colour. The fraction of HERGs increases with redshift, as does the fraction of sources in galaxies with lower stellar masses. We find that the fraction of galaxies that host LERGs is a strong function of stellar mass as it is in the local Universe. This, combined with the strong negative evolution of the LERG luminosity functions over this redshift range, is consistent with LERGs being fuelled by hot gas in quiescent galaxies.

Key words: galaxies: active – galaxies: evolution – radio continuum: galaxies.

1 INTRODUCTION

The evolution of radio-loud active galactic nuclei (RL AGN) is closely entwined with that of their host galaxies and the central supermassive black holes that power them. The ability of the expanding radio lobes of RL AGN to do work on the surrounding intra-cluster medium provides an important 'feedback' mechanism by which a central black hole can regulate or extinguish star formation in its parent galaxy (see e.g. Best et al. 2006, 2007; Bower et al. 2006; Croton et al. 2006; Fabian, Celotti & Erlund 2006; Cattaneo et al. 2009). Over recent years, RL AGN have come to be classified based on their Eddington-scaled accretion rates, with sources on either end of the scale exhibiting very different

---

★ E-mail: w.williams5@herts.ac.uk

characteristics (Best & Heckman 2012; Son et al. 2012; Russell et al. 2013; Gürkan, Hardcastle & Jarvis 2014; Mingo et al. 2014; Fernandes et al. 2015).

RL AGN with high Eddington-scaled accretion rates experience radiatively efficient accretion of cold gas via an accretion disc (e.g. Shakura & Sunyaev 1973) and therefore appear as 'quasars' (Silk & Rees 1998), with emission across the electromagnetic spectrum (e.g. Barthel 1989; Antonucci 1993; Urry & Padovani 1995). In the literature, these are variously referred to as 'cold mode' or 'radiative mode' or 'high-excitation' sources because they are characterized by strong optical emission lines. They are typically hosted by lower mass, bluer galaxies in less dense environments (e.g. Tasse et al. 2008b; Janssen et al. 2012). While the most powerful radio sources tend to be high-excitation radio galaxies (HERGs), they are in fact found at all radio powers (Best & Heckman 2012). Due to their strong evolution with redshift this mode is likely important in cutting off star formation at high redshifts and thus setting up the tight black hole versus bulge mass relation that is observed locally (Magorrian et al. 1998). At the low, or radiatively inefficient, end of the Eddington-scaled accretion rate spectrum radio galaxies are found to have no or weak emission lines (Hine & Longair 1979; Laing et al. 1994; Jackson & Rawlings 1997) and are thought to be fuelled by hot gas accreting directly on to the supermassive black hole (Hardcastle, Evans & Croston 2007), e.g. via advection-dominated accretion flows (e.g. Narayan & Yi 1995). Typically hosted by higher mass, redder galaxies and occurring in more dense environments (Best et al. 2005a), these sources have no mid-infrared (MIR) emission or optical obscuration from dust (Whysong & Antonucci 2004; Ogle, Whysong & Antonucci 2006), they have no accretion-related X-ray emission (Evans et al. 2006; Hardcastle, Evans & Croston 2006) and their radio powers tend to be low. Forming the bulk of the population in the local Universe, these low-excitation radio galaxies (LERGs) are otherwise referred to as 'hot mode', 'radio mode', or 'jet mode' in the literature. LERGs have a direct link between the black hole and its hot gas fuel supply and can maintain elliptical galaxies at lower redshifts as 'old, red, and dead' (e.g. Best et al. 2006) and can prevent strong cooling flows in galaxy clusters (e.g. Fabian et al. 2006). For a comprehensive review on the current understanding of the HERG/LERG populations, see Heckman & Best (2014) and McNamara & Nulsen (2012) and references therein.

It is well known that, within the local Universe ($z \lesssim 0.3$), the RL fraction, i.e. the fraction of galaxies hosting an RL AGN, is strongly dependent on the stellar mass of the host galaxies ($f_{\rm RL} \propto M_*^{2.5}$, Best et al. 2005b; Tasse et al. 2008b; Janssen et al. 2012; Simpson et al. 2013), increasing to >30 per cent at stellar masses above $5 \times 10^{11}\,{\rm M}_{\odot}$ for radio luminosities $>10^{23}\,{\rm W\,Hz}^{-1}$. However, this mass dependence of the entire population is driven by that of LERGs that dominate the RL AGN population at these redshifts (Best et al. 2006). The RL fraction for HERGs has a much shallower mass dependence, $f_{\rm RL} \propto M_*^{1.5}$ (Janssen et al. 2012). Furthermore, Janssen et al. (2012) have shown that the fraction of RL AGN for the two classes have different dependencies not only on the stellar mass of the host galaxies but also on properties such as colour and star formation rate (SFR): red (passive) galaxies are a factor of a few times more likely to host lower power LERGs than blue (star-forming) galaxies of the same stellar mass; blue galaxies show a higher probability of hosting HERGs at all radio luminosities than red galaxies; and for blue galaxies, the likelihood of hosting either radio AGN type is a strong positive function of the SFR. It is clear that the presence of cold, star-forming gas in a galaxy clearly enhances the probability of its central BH becoming an RL AGN. This means that some LERG activity, especially at high radio luminosities is not solely related to hot halo gas accretion and is consistent with it being produced at low accretion rates by either hot or cold gas (Heckman & Best 2014). A key open question is how the radio galaxy populations and RL fraction for each depend on host galaxy masses and colours at higher redshifts. As a first step, in studying the RL fraction at $z \approx 1$–2, Williams & Röttgering (2015) found more than an order of magnitude increase in the fraction of lower mass galaxies ($M_* < 10^{10.75}\,{\rm M}_{\odot}$) that host RL AGN with radio powers $P_{1.4\,{\rm GHz}} > 10^{24}\,{\rm W\,Hz}^{-1}$ compared to the local Universe.

Optical spectra are the key discriminator between HERGs and LERGs. Based on SDSS spectroscopy, Best & Heckman (2012) built the largest sample of HERGs/LERGs in the local Universe, but this is harder to do at higher redshifts. Best et al. (2014, hereafter B14) provided the first sample of intermediate redshift ($z < 1$) objects that are spectroscopically classified as HERGs and LERGs. Since then, Pracy et al. (2016) have classified a much larger sample, but still probing only out to a redshift of about one. To build large high-redshift samples requires a method independent from spectroscopy for the separation of HERGs and LERGs. Quasar-selection techniques based on MIR colours (Stern et al. 2005; Donley et al. 2012; Stern et al. 2012) fail to select all high excitation sources and selections based on X-ray emission alone (e.g. Hickox et al. 2009) miss obscured and weaker sources. In this paper, we classify a sample of RL AGN as HERGs and LERGs on the basis of their broad-band spectral energy distributions (SEDs) and study the RL fractions, radio luminosity functions (LFs) and colour and mass dependencies for the two classes of RL AGN at intermediate redshifts of $0.5 \le z < 2$. Preliminary results were presented in Williams et al. (2015).

This paper is structured as follows. The LOw Frequency ARray (LOFAR) 150-MHz radio data are described in Section 2 and the multiwavelength data sets and catalogues we use are described in Section 3. In Section 4, we use SED fitting to determine photometric redshifts and galaxy parameters for the sample of optical galaxies. Section 5 describes our method for identifying optical counterparts to the LOFAR radio sources. In Section 6, we describe further SED fitting to classify sources from this RL AGN sample as HERGs and LERGs. Section 7 describes the selection of a well-defined subsample of RL AGN and presents an analysis of the properties of the RL AGN, including the RL fraction and LFs of HERGs and LERGs. Throughout this paper, we use AB magnitudes and a concordance cosmology with $\Omega_M = 0.3$, $\Omega_\Lambda = 0.7$, and $H_0 = 70\,{\rm km\,s}^{-1}\,{\rm Mpc}^{-1}$. The spectral index, α, is defined as $S_\nu \propto \nu^\alpha$, where S is the source flux density and ν is the observing frequency. We assume a spectral index of -0.7 unless otherwise stated.

2 RADIO DATA

The low-frequency radio data are described by Williams et al. (2016), but we provide a brief summary here. The 8 h observation was taken with the LOw Frequency ARray (LOFAR; van Haarlem et al. 2013) using the high band antennae and covering the frequency range of 130–169 MHz, with a central frequency of ≈150 MHz. Particular care was taken in the calibration and imaging to correct for direction-dependent effects (DDEs) caused by the ionosphere and imperfect knowledge of the LOFAR station beam shapes. This DDE calibration and imaging was achieved with the 'Facet' calibration scheme presented by van Weeren et al. (2016). The resulting image covers $19\,{\rm deg}^2$, with an rms noise of ≈120–150 $\mu{\rm Jy\,beam}^{-1}$. Assuming a spectral index of -0.7, the sensitivity of this map is

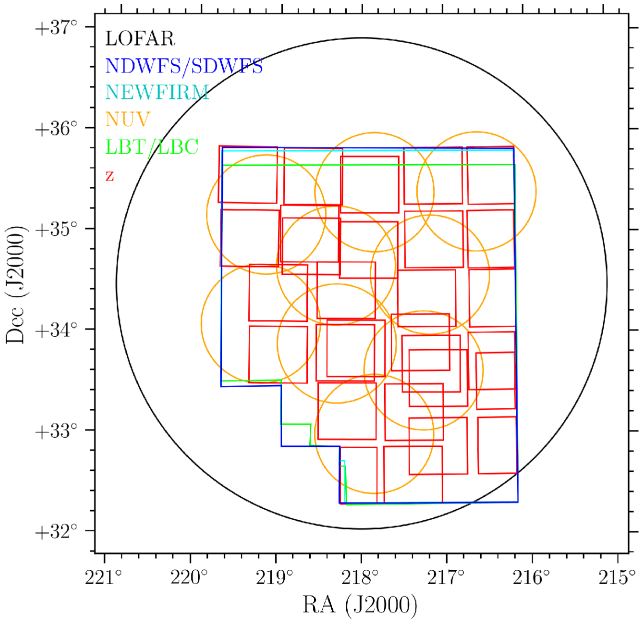

Figure 1. Coverage diagram for the Boötes field. The black circle shows the LOFAR 150-MHz coverage. The blue polygon shows the main *I*-selected point spread function (PSF)-matched catalogue region, which is covered completely by both the NDWFS ($B_W RIK$) and SDWFS (3.6, 4.5, 5.8, and 8.0 µm). It covers a total of 9.2 deg^2, when regions contaminated by bright stars are excluded. The red squares show the *z*Boötes coverage, which has some gaps. The orange circles show the *GALEX* NUV coverage. There is a small area not covered by the NEWFIRM survey (J, H, and K_s, shown in cyan) and the LBT/LBC survey ($U_{\rm spec}$, and Y, shown in light green).

comparable to the 28 µJy beam^{-1} rms of the WSRT 1.4 GHz image made by de Vries et al. (2002). However, LOFAR's superior resolution of 5.6 × 7.4 arcsec (compared to 13 × 27 arcsec at 1.4 GHz), combined with its positional accuracy of <1 arcsec, makes it significantly better for the optical identification of the radio sources. The LOFAR 150-MHz radio source catalogue contains 6276 sources detected with a peak flux density threshold of 5σ, where σ is the local rms noise. The radio coverage is shown as a circle in Fig. 1.

3 MULTIWAVELENGTH DATA

The Boötes field is amongst the widest of the famous deep extragalactic fields and was first observed as one of two fields within the National Optical Astronomy Observatory (NOAO) Deep Wide Field Survey (NDWFS; Jannuzi et al. 1999). Since then it has been surveyed across the electromagnetic spectrum. We describe here the surveys and data sets that are used in this work.

3.1 Combined photometry catalogue

The primary catalogue that we make use of is the combined *I*-band-selected PSF-matched photometry catalogue presented by Brown et al. (2007, 2008). This catalogue includes 15 bands spanning 0.14–24 µm and combines several different surveys. These include the original optical (B_W, R, and I) and the NIR (K) survey, surveys with the *Spitzer Space Telescope* at 3.6, 4.5, 5.8, and 8.0 µm (SDWFS; Ashby et al. 2009), and 24 µm (MAGES; Jannuzi et al. 2010), NUV and FUV surveys from *GALEX*, and deeper J-, H-, K_s-, and z-band surveys.

Brown et al. (2007) have constructed a combined PSF-matched catalogue by regridding and smoothing the individual released survey images to a common scale so that the stellar point spread function (PSF) is a Moffat profile with a full width at half-maximum (FWHM) of 1.35 arcsec and $\beta = 2.5$ for the B_w, R, I, Y, H, K, and K_s bands and with an FWHM of 1.6 arcsec for the u, z and J bands. PSF fluxes are extracted from these images for all the sources in the *I*-band using SExtractor (Bertin & Arnouts 1996). For the remaining bands, aperture fluxes were extracted. Regions surrounding very extended galaxies and saturated stars were excluded. The final sample area is 9.2 deg^2. The geometry of the Boötes field is shown in Fig. 1.

3.2 Additional multiwavelength coverage

Boötes is part of the *Herschel* Multi-tiered Extragalactic Survey (HerMES; Oliver et al. 2012), which includes photometry using the Spectral and Photometric Imaging Receiver (SPIRE; Griffin et al. 2010) instrument at 250, 350, and 500 µm. Within HerMES, Boötes has 'level 5' coverage of 3.25 deg^2 to 5σ noise levels of 13.8, 11.3, and 16.4 mJy and 'level 6' coverage of 10.57 deg^2 to 5σ noise levels of 25.8, 21.2, and 30.8 mJy. In this paper, we use the maps (Levenson et al. 2010) from the fourth data release (DR4).

The AGN and Galaxy Evolution Survey (AGES; Kochanek et al. 2012) has provided redshifts for 23 745 galaxies and AGN across 7.7 deg^2 of the Boötes field. The AGES spectra were obtained for random sparse samples of normal galaxies brighter than $m_I < 20$ mag (significantly deeper than SDSS). Additional samples of AGN, selected in the radio, X-ray, IRAC MIR, and MIPS 24 µm, were targeted to fainter limiting magnitudes ($m_I < 22.5$ mag for point sources). The survey used the Hectospec instrument (Fabricant et al. 2005) on the MMT to obtain 3700–9200 Å spectroscopy at a spectral resolution of 6 Å ($R \approx 1000$ Kochanek et al. 2012; Cool et al. 2012). The median redshift of the galaxies in the survey is $\langle z \rangle = 0.3$, with 90 per cent of the redshifts in the range of $0.085 \lesssim z \lesssim 0.66$. However, the spectroscopic redshift completeness for the matched LOFAR sources believed to be at $z > 1$ is less than 50 per cent. For this reason, we derive photometric redshifts, described in the following section. AGES also provides photometric redshifts, calculated using the LRT code by Assef et al. (2010) that fits a combination of an early-type, late-type, star-forming, and (obscured) AGN to the observed broad-band SEDs. The photometry they used is a subset of that used in this work.

4 SED FITTING

For the 888 956 optical sources in the Brown et al. (2007) PSF-matched photometry catalogue with $m_I \leq 24$ mag and FLAG_DEEP = 1, and for which we have either spectroscopic or photometric redshifts, we fit their SEDs to determine galaxy parameters, including stellar mass, SFRs, and colours. Prior to any fitting, the photometry catalogue was filtered to remove catastrophic outliers, i.e. flux densities lower (higher) than 2.5 mag (1 mag) compared to the two adjacent filters were flagged (and not used in later fitting). These cut-offs were chosen to be sufficiently extreme not to flag any reasonable spectral emission or absorption features and by comparing to two adjacent filters bona fide spectral breaks are not flagged. About 1–2 per cent of the photometry points were flagged in this way.

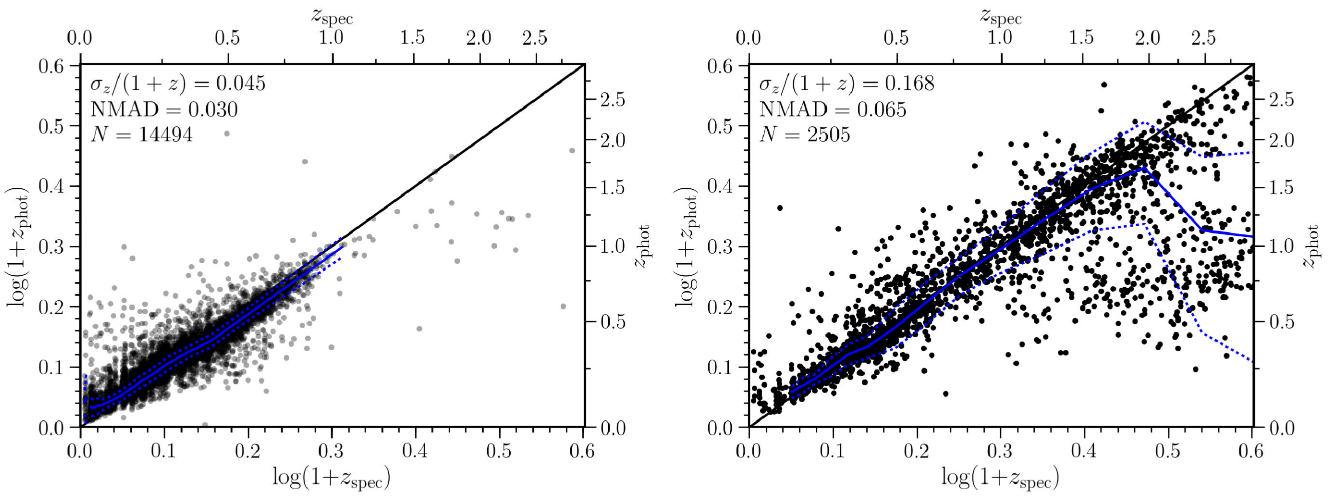

Figure 2. Photometric redshifts from the Boötes *I*-selected catalogue versus spectroscopic redshifts from the AGES catalogue. Left: Only galaxies not indicated as AGN in the AGES catalogue are plotted. Right: Sources indicated to be AGN by the AGES SED fitting. The solid and dotted blue curves show, respectively, the median and rms dispersion of $\delta z = (z_{\rm phot} - z_{\rm spec})/(1 + z_{\rm spec})$, within 11 logarithmic-spaced bins across the spectroscopic redshift range.

4.1 Photometric redshifts

Photometric redshifts are provided by the hybrid photometric redshift method presented by Duncan et al. (2017) and Duncan et al. (2018), based on the Brown et al. (2007) photometry catalogue. The redshifts are derived by combining template-based estimates with additional Gaussian process estimates (Almosallam et al. 2016a; Almosallam, Jarvis & Roberts 2016b) trained for subsets of the sample population, specifically infrared-, X-ray-, and optically selected AGN as well as the remaining galaxy population. The three different template-based estimations were calculated following the methodology presented by Duncan et al. (2018), using the EAZY software (Brammer, van Dokkum & Coppi 2008) and three different template sets: one set of stellar-only templates, the EAZY default library (Brammer et al. 2008), and two sets including both stellar and AGN/QSO contributions, the XMM-COSMOS templates (Salvato et al. 2008) and the Atlas of Galaxy SEDs (Brown et al. 2014).

The multiple individual $z_{\rm phot}$ estimates were then combined using a Hierarchical Bayesian method (Dahlen et al. 2013), as an alternative to a straight addition of the probability distributions of the $z_{\rm phot}$ estimates. The main advantage of this method is that it determines the consensus probability $P(z_{\rm phot})$ for each object, given the possibility that the individual measured probability distributions may be wrong. These results were also optimized using zero-point offsets calculated from the spectroscopic redshift sample and the posterior redshift predictions calibrated such that they accurately represent the uncertainties in the estimates.

4.1.1 Comparison with AGES redshifts

While the quality of the photometric redshifts is analysed in detail by Duncan et al. (2017), we provide here a brief overview because the quality of the photometric redshifts is fundamental for the subsequent analysis. In Fig. 2, we show a comparison between the Duncan et al. (2017) $z_{\rm phot}$ and $z_{\rm spec}$ for the sources with good AGES spectroscopic redshifts (with a signal to noise >5). In general, the photometric redshifts compare well to the spectroscopic redshifts, although we note that this comparison is primarily from galaxies at $z_{\rm spec} < 1.0$. Galaxies that are $>3\sigma$ outliers from the one-to-one relation based on their redshift errors from the consensus $z_{\rm phot}$ estimates are considered catastrophic outliers, the fraction of which is 1.2 per cent. As a measure of the accuracy of the photometric redshifts, we consider two quantities, computed after excluding the catastrophic outliers. The first goodness measure is the standard dispersion, $\sigma_z/(1+z)$, defined by

$$\left(\frac{\sigma_z}{1+z}\right)^2 = \frac{1}{N}\sum_{i=1}^{N}\left(\frac{z^i_{\rm phot} - z^i_{\rm spec}}{1+z^i_{\rm spec}}\right)^2. \qquad (1)$$

The second is the normalized median absolute deviation (NMAD) of the residuals, defined as NMAD$(\Delta z) = 1.48 \times$ median(Δz), where $\Delta z = (z_{\rm phot} - z_{\rm spec})/(1 + z_{\rm spec})$. We measure $\sigma_z/(1+z) = 0.11$ and NMAD = 0.028. It is well known that photometric redshifts are poorly determined for AGN (e.g. Brodwin et al. 2006; Rowan-Robinson et al. 2008; Assef et al. 2010), and should preferably be fit using different methods (e.g. Salvato et al. 2009, 2011). We compare the $z_{\rm phot}$ and $z_{\rm spec}$ for normal galaxies and AGN separately in Fig. 2. For this, we use the sources flagged as AGN by Assef et al. (2010), which is based on their having a significant contribution by an AGN SED template. Excluding the galaxies selected as AGN in AGES, we find that the photometric redshifts are more accurate for normal galaxies, with $\sigma_z/(1+z) = 0.045$ and NMAD = 0.030. Considering only the AGES AGN, we find $\sigma_z/(1+z) = 0.17$ and NMAD = 0.065. This is comparable with the redshifts determined by Assef et al. (2010), with $\sigma_z/(1+z) = 0.04$ for normal galaxies and $\sigma_z/(1+z) = 0.18$ for point-like AGN. For comparison, the most accurate photometric redshifts available in the literature typically have $\sigma z/(1+z) \lesssim 0.01$ (e.g. Ilbert et al. 2009; Muzzin et al. 2013), but using 30 bands of broad, intermediate, and narrow width.

4.2 Stellar masses, SFRs, and rest-frame colours

Stellar population parameters are determined by fitting galaxy SEDs using the FAST code (Kriek et al. 2009), based on the Bruzual & Charlot (2003) models. We assume solar metallicity, a Chabrier (2003) initial mass function (IMF), and a Calzetti et al. (2000) dust extinction law. The template SEDs are constructed in the standard way (see e.g. Muzzin et al. 2013), assuming exponentially declining star formation histories (SFHs) of the form SFR $\propto \exp(-t/\tau)$, where t is the time since the onset of star formation and τ is the *e*-folding star formation time-scale in units of Gyr. All galaxies are fitted assuming their redshift is the $z_{\rm spec}$ from AGES or, where none is available, the consensus $z_{\rm phot}$ estimate. In all, four parameters are determined per galaxy: τ, t, A_V (the *V*-band extinction), and a normalization. The stellar mass (M_*) is then determined from mass-to-light ratio of the best-fitting SED multiplied by the best-fitting normalization of the SED.

Rest-frame colours are derived using InterRest (Taylor et al. 2009) with the consensus $z_{\rm phot}$ estimates. We determine colours for the $^{0.1}u$ and $^{0.1}r$ bands, defined as the AB magnitudes in the SDSS *u* and *r* bands at $z = 0.1$. These colours allow straightforward comparison to SDSS results (e.g. Blanton et al. 2003a,b,c; Kauffmann et al. 2003).

5 OPTICAL IDENTIFICATION OF RADIO SOURCES

In this section, we describe the identification of optical counterparts, from the *I*-band-selected optical catalogue described in Section 3, matched to the LOFAR radio sources, described in Section 2. We use a statistical technique to determine the probability that an *I*-band optical source is the true host of a particular radio source. Prior to this, we inspect the radio-optical images (radio contours of each radio source overlaid upon the corresponding *I*-band image) and classify their radio morphologies into the different categories described below.

5.1 Visual classification

In order to identify the host galaxies of radio sources, the true location of the host galaxy with respect to the radio source should be known. Following Best et al. (2003) and Tasse et al. (2008a), we determine a strong subjective prior on this location for each source by visually inspecting all the radio-optical images and dividing them into the following classes based on the radio morphology:

Class 1: For these sources, the radio emission is expected to be coincident with the optical emission (although the optical emission may be below the detection limit). This occurs in sources such as starburst galaxies, compact core-dominated radio sources or radio sources where the radio core can be clearly identified. In these cases, the errors on the radio and optical positions can be used in a statistical way to identify the optical counterpart of each radio source. We consider all relatively small (usually single-component) sources in this category, even if they are slightly resolved and take into account the larger uncertainties on the radio positions in the likelihood ratio (LR) analysis in the next section. We note that some radio sources appear resolved because of some bandwidth- and time-smearing in the LOFAR image (see Williams et al. 2016).

Class 2: In the case that no radio core is identified (such as for classical double lobe FRII (Fanaroff & Riley 1974) radio sources, only a weak prior can be considered for the optical host position. The position of the host and associated errors are estimated based on the flux-weighted centroid of the multiple Gaussian fitting components, as described in more detail by Best et al. (2003). For very large such sources, the error regions become large and these are then considered as Class 3 sources below.

Class 3: When the radio source is large or very asymmetric, the flux-weighted radio centroid and associated errors can be very far from the real optical host. We use the combination of radio morphology and optical properties (such as an elongated lobe pointing to a bright optical object), to infer the position of the optical counterpart. These sources are matched (or left without an optical match where none is obvious) visually on a case-to-case basis and the statistical method described below cannot be used.

Class 4: These are clearly resolved and diffuse radio sources whose morphology is not suggestive of jets. This includes 'radio haloes' and 'relics', typically found in clusters. These sources have been excluded from further analysis.

Class 5: When the radio source overlaps a bright saturated source, we have classified the source as Class 5. These sources likely have contaminated photometry and have been excluded in further analysis.

5.2 Likelihood ratio

For the Class 1 and 2 sources, we employ a statistical method to determine the optical counterparts to the radio source. We use the LR method (Richter 1975) to determine the probability that an *I*-band optical source is the true counterpart of a particular radio source. The LR method has been further developed by Prestage & Peacock (1983), Benn (1983), Wolstencroft et al. (1986), and Sutherland & Saunders (1992). Here, we use the methodology outlined by Tasse et al. (2008a). The probability that an optical *I*-band source is the true optical counterpart of a given radio source is determined from the LR (Sutherland & Saunders 1992; Tasse et al. 2008a), defined as

$$\mathrm{LR}(r, m) = \frac{\theta(< m)\exp\left(-0.5r^2\right)}{2\pi\sigma_\alpha\sigma_\delta\rho(< m)}, \tag{2}$$

where m is the *I*-band magnitude of the optical candidate, $\theta(<m)$ is the pre-determined probability that a radio source has an observed optical counterpart with magnitude $<m$, and $\rho(<m)$ is the surface number density of objects with magnitude $<m$. The parameter r is the uncertainty-normalized angular distance between the radio core and the optical host candidate, defined as $r^2 = (\Delta\alpha/\sigma_\alpha)^2 + (\Delta\delta/\sigma_\delta)^2$, where Δ is the positional difference, σ is the uncertainty, and α and δ are the right ascension and declination, respectively. For each α and δ, the uncertainty is the quadratic sum of the uncertainty on the radio position, $\sigma_{\rm radio}$, and on the optical position, $\sigma_{\rm opt}$. We adopt an optical astrometry accuracy of $\sigma_{\rm opt} \approx$ 0.35 arcsec, independent of the magnitude m_I. The accuracy of the radio position, $\sigma_{\rm radio}$, is different for every source and depends on the signal-to-noise ratio and the Gaussian fitting parameters (Williams et al. 2016). The probability $P_{\rm id}(i)$ of the ith candidate being a true identification is

$$P_{\rm id}(i) = \frac{\mathrm{LR}_i(r, m)}{\sum_j LR_j(r, m) + [1 - \theta(m_{\rm lim})]}, \tag{3}$$

where $\theta(m_{\rm lim})$ is the fraction of radio sources having detected optical counterparts at the limiting magnitude of the survey, i refers to the candidate under consideration and j runs over the set of all possible candidates. We estimate the association probability assuming that θ and ρ depend only on the object magnitude m, which is taken as the *I*-band magnitude of the optical candidate. For each radio source, we calculate the density function $\rho(m)$ within 2 arcmin of the radio source centroid, in order to account for the variation of the surface density with position, or clustering of optical sources. To estimate the function $\theta(<m)$, we follow the methodology of Tasse et al. (2008a). This involves simulating random radio and optical catalogues with a known fraction of radio-optical matches and comparing the simulated radio-optical separation distribution to the real distribution. We consider discrete *I*-band magnitude cuts in the interval $13 < I < 24$ with an increment $\Delta m_I = 0.2$. For

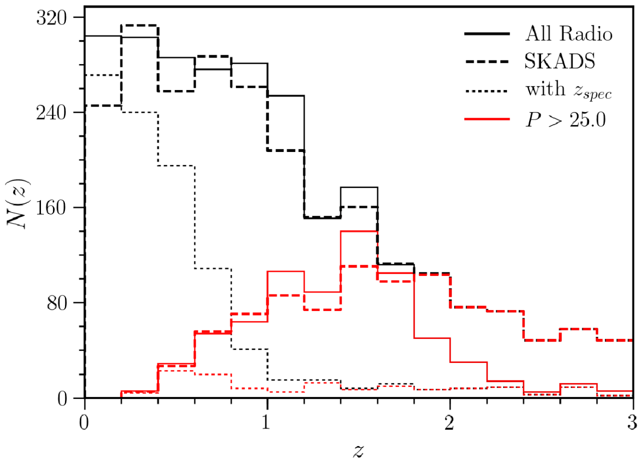

Figure 3. Redshift distribution. The high-power sample defined in Section 7.1 is plotted in red and the full radio-optical sample is plotted in black. The dashed lines show the predictions from the SKA-simulated skies (Wilman et al. 2008). The spectroscopic redshift distribution for each is plotted with dotted lines.

each of these cuts, an optical catalogue with uniformly distributed positions is generated. A corresponding radio catalogue is generated assuming a given fraction, $\theta(<m)$, of radio sources have an optical counterpart (i.e. the same position as a source in the optical catalogue), while the remainder have uniformly distributed positions. All the radio and optical positions are then shifted by Gaussian-distributed offsets in right ascension and declination with the standard deviations given by the respective positional uncertainties. The distribution of the angular distance between radio sources and their closest object in the optical catalogue is then computed and compared to the real distribution through a Kolmogorov–Smirnov test. The fraction, $\theta(<m)$, corresponding to the maximum Kolmogorov–Smirnov probability is retained. For each *I*-band magnitude cut, the test is repeated 10 times, to estimate an error on $\theta(<m)$.

5.3 Radio-optical match results

Of the 6267 sources in the LOFAR 150-MHz catalogue, 3894 lie within the boundary of the optical catalogue and may therefore have potential optical counterparts. Based on the visual inspection of the radio and optical images, we separated eight sources that had been grouped by the original source detection algorithm (i.e. where PYBDSF grouped two Gaussians into one source, but the optical images suggest these are two Class 1 sources instead of one Class 2 source). The majority, 3403, of these sources were classified as Class 1 (87 per cent), 177 sources (4.5 per cent) were classified as Class 2, 4 sources (<1 per cent) were classified as Class 3, and 24 sources (<1 per cent) were classified as Class 4 (diffuse sources) or Class 5 (sources with bad optical photometry). Some examples of the Class 1 and 2 sources with LR-matched optical sources are shown in Figs A1 and A2, respectively, in Appendix A. In the following analysis for the Class 1 and 2 sources with LR-matched optical sources, we select only the match with the maximum probability, where there is more than one possible optical identification, and only the sources with $P_{\rm id} > 0.7$. Of the total of 3902 sources, we found at least one optical counterpart for 2428 sources (76 per cent) of which 2835 have $m_I < 24$ mag.

Fig. 3 shows the redshift distribution of all the matched radio-optical sources. A small number (30) of sources, not shown, have photometric redshifts in the range of $3 < z < 6$ are not shown here. We show also the predictions from the SKA-simulated skies (Wilman et al. 2008) constrained by our observed coverage area and rms distribution. The distributions of the simulated sources are in very good agreement with the observed distributions, at least up to $z < 2$. Above this redshift, there are indications of incompleteness in our matched sample as sources fall below our optical detection threshold. The dotted lines in this plot show the distribution of sources with spectroscopic redshifts from AGES – the low completeness of which motivates the need for a complete sample with photometric redshifts. However, due to the AGES selection criteria (see Kochanek et al. 2012), most of the sources at $z > 1$ with spectroscopic redshifts are AGN. Thus, the sources most likely to have poor photometric redshifts are more likely to have spectroscopic redshifts. Throughout the rest of this paper, we adopt the $z_{\rm spec}$ from AGES where possible, otherwise we use the consensus $z_{\rm phot}$ estimates. The radio power versus redshift for these sources is shown in Fig. 4.

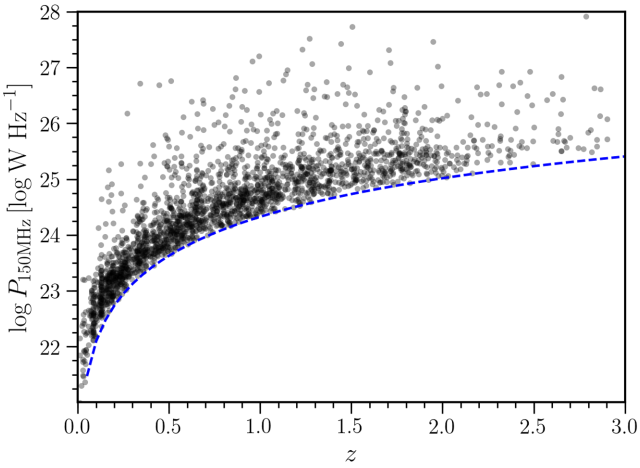

Figure 4. Distribution in the radio power versus redshift plane of the matched radio-optical sources. The dashed blue line shows the radio power corresponding to a flux density limit of 0.5 mJy beam^{-1}.

5.3.1 Contamination

In order to estimate the level of contamination by random matches, we generated 15 radio catalogues by randomizing the positions of the sources in the real radio catalogue. We then cross-matched these 15 random radio catalogues with the optical sources in the same manner as described in the previous section. The distributions of optical identifications in stellar mass are plotted in Fig. 5. The contamination is high for sources with low stellar masses, likely driven by the higher surface density of faint optical galaxies with low stellar masses. The total contamination is ≈10 per cent for all the sources with stellar masses $M_* < 10^{12}\,{\rm M}_\odot$. However, for sources with stellar masses $M_* < 10^9\,{\rm M}_\odot$ the contamination exceeds 90 per cent. We therefore do not consider optical identifications with objects with stellar masses below this value in later analysis.

6 PANCHROMATIC SED FITTING

While Gürkan et al. (2014) have suggested that for high radio luminosities, a single cut in 22 μm flux can be used to separate LERGs and HERGs, this may not be the case at lower luminosities (Janssen et al., in preparation). We therefore attempt to separate these sources based on further SED fitting to determine the relative contributions

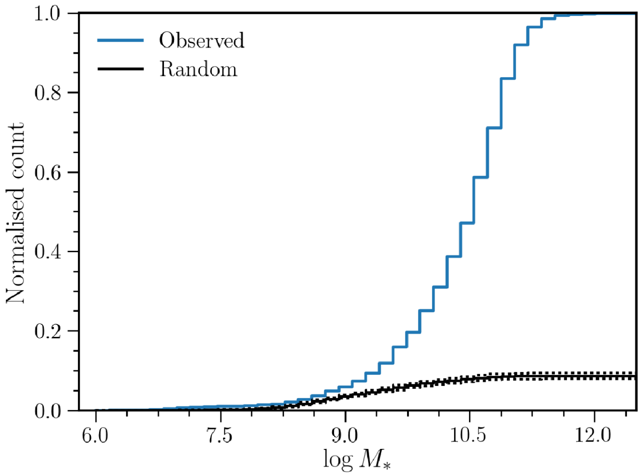

Figure 5. Stellar mass distributions for the observed sample (blue) and the 15 random radio catalogues (black). The total contamination is ≈10 per cent.

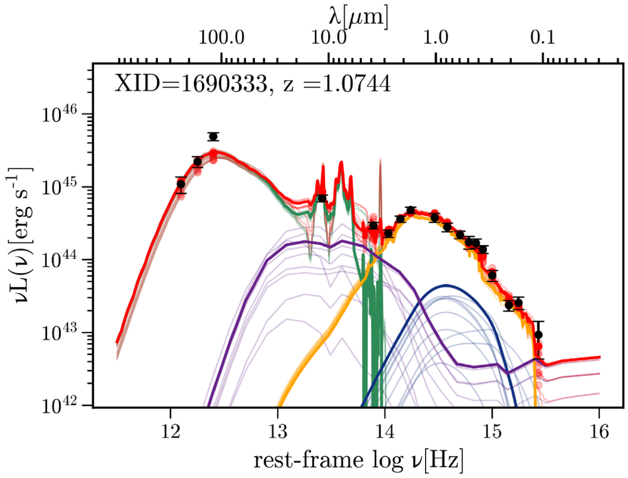

Figure 6. Example AGNFITTER SED fit showing the total model SEDs in red, and the AGN torus (purple), starburst (green), galaxy (yellow), and blue bump (blue) components. Ten realizations from the model parameters' posterior probability distributions are plotted giving an indication of the uncertainties in the fitted components. The red points show the total SEDs integrated across the filter bandpasses, and the black points with errorbars show the observed luminosities.

of the AGN and galaxy components at IR wavelengths. For this fitting, we have included the far-infrared (FIR) fluxes of these sources at 250, 350, and 500 μm by matching to the HerMES catalogue for the Boötes Field (Oliver et al. 2012). The *Herschel* fluxes were found by extracting the flux densities and errors directly from the DR4 maps at the optical source positions in the manner described by Hardcastle et al. (2013). The FIR fluxes are particularly important here to constrain the separation between the star-forming and AGN components. In order to decompose the SEDs of all the matched radio-optical sources, we fit all the available multiwavelength photometry, including FIR, using the MCMC-based algorithm AGNFITTER (Calistro Rivera et al. 2016). Calistro Rivera et al. used AGNFITTER to separate star-forming galaxies and AGN. An example fitted SED is shown in Fig. 6. We note here that this fitting is dependent on the photometric redshifts, and we have incorporated the full photometric redshift probability density functions (PDFs) in the AGNFITTER analysis. For each source with a photometric redshift, we produce 100 samples from the photometric redshift PDF, run AGNFITTER for each sample, and combine the PDFs for the individual AGNFITTER parameters. For sources with spectroscopic redshifts, we use those as a single sample.

The advantage of using AGNFITTER is that it infers the posterior PDFs of the fitting parameters. This allows correlations and degeneracies amongst parameters to be recognized and allows for a robust calculation of the uncertainties for the inferred parameter values, and allows us to fold in the photometric redshift PDFs into the analysis. As described in Calistro Rivera et al. (2016) and following their nomenclature, the total model in AGNFITTER is the sum of the emission from the host galaxy and nuclear AGN. The host galaxy emission is represented by both stellar emission (GA) and the reprocessed light from cold/warm dust (starburst component; SB[1]). Similarly, the AGN emission is represented by the combination of an UV/optical accretion disc component (Big Blue Bump; BB) and a hot dust torus component (or other obscuring structure, TO). The GA component consists of the standard stellar population synthesis models of Bruzual & Charlot (2003) with a Calzetti et al. (2000) dust extinction law covering a broad range in SFRs, including quiescent galaxies. The SB models used are the templates from Chary & Elbaz (2001) and Dale & Helou (2002), again covering a range in SFRs. A fit to a quiescent galaxy will yield a negligible SB component. The stellar templates come from the models of Bruzual & Charlot (2003) with a Chabrier (2003) initial mass function. The nuclear hot-dust torus models are taken from Silva, Maiolino & Granato (2004).

A small fraction of sources (22, ≈1 per cent) have very poor fits, i.e. have AGNFITTER likelihood values <-100. These are excluded in further analysis. Some examples of the AGNFITTER SEDs with components in the three redshift intervals are shown in Appendix B in Figs B1 and B2 for sources with good-quality fits (quantified by likelihood values close to -1) and in Fig. B3 for sources with poor fits (quantified by likelihood values $\lesssim -20$).

We compare the stellar masses and SFRs returned by AGNFITTER to those we have derived using FAST (see Section 4.2). This comparison is shown in Fig. 7. We do not use SFRs in the subsequent analysis, but do use the fitted starburst components from AGNFITTER in classifying radio sources as star forming. While the two codes are used to fit the same data (with the exception that the longest wavelength MIR and FIR data is included for the AGNFITTER fits), the fitting methods and templates, specifically the inclusion of the AGN components in AGNFITTER, used are independent. AGNFITTER returns SFRs measured both from the stellar templates in the optical-UV, like FAST, as well as in the IR. In the comparison here, we use the AGNFITTER SFRs inferred from the total IR luminosities, because these are related to the total SB IR luminosity used in the following section to classify star-forming galaxies. Although not shown here, there is good agreement between the IR and optical SFRs derived by AGNFITTER, with a few extremely large optical SFRs, like those observed in the FAST SFRs in Fig. 7. Stellar-template-derived optical-UV emission SFRs are prone to significant dust extinction and can be less reliable.

---

[1] While this is referred to as a 'starburst' component in AGNFITTER, it is more generally the cold/warm dust emission in star-forming regions and is not restricted to the most extreme SFRs. However, we keep the 'SB' abbreviation in the following to be clear that we are referring to the cold/warm dust AGNFITTER templates.

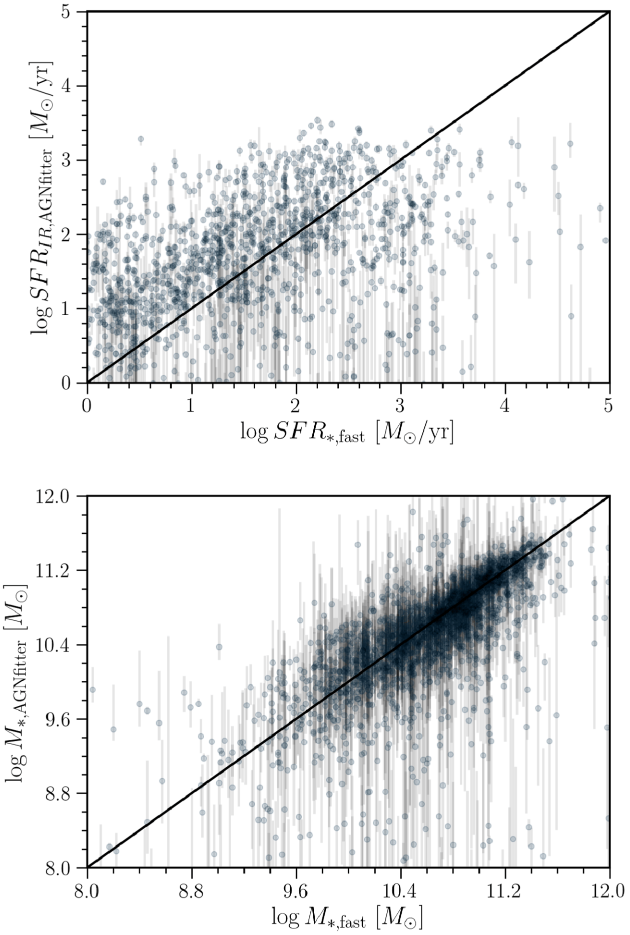

Figure 7. Comparison between SFR (top) and stellar mass (bottom) determined by FAST and AGNFITTER.

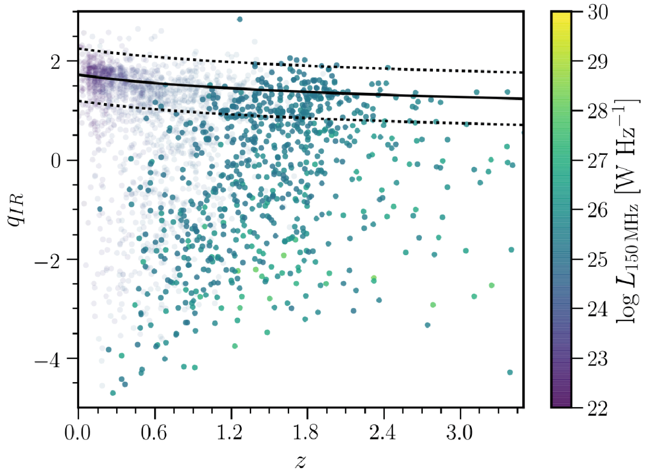

Figure 8. FIR-radio correlation, q_{IR}, computed from the IR luminosities, L_{IR}, integrated from the AGNFITTER cold dust component. The solid and dashed lines show the $q_{\mathrm{IR}} = 1.72(1 + z)^{-0.22}(\sigma = 0.529)$ FIR-radio correlation from Calistro Rivera et al. (2017). The larger points show the radio sources with $P_{150\,\mathrm{MHz}} \geq 10^{25}$ W Hz^{-1}.

6.1 Star formation

The radio power-redshift distribution (Fig. 4) shows that we are mostly sensitive to high power sources at intermediate redshifts, while at low redshifts the opposite is true. If the radio emission is driven by star formation alone, then at radio powers $P_{150\,\mathrm{MHz}} \gtrsim 10^{25}$ W Hz^{-1} (corresponding to $P_{1.4\,\mathrm{GHz}} \gtrsim 10^{24}$ W Hz^{-1}, for a spectral index of -0.7), the required SFR is in excess of 25 M$_\odot$ yr^{-1} (Condon 1992). This is not unreasonable for star-forming galaxies at these intermediate redshifts, so we may expect some contamination of our RL AGN sample by star-forming galaxies. To explore this further, we consider the total SB IR luminosities, L_{IR}, defined as the total SB IR luminosity, L_{IR}, integrated over the rest-frame wavelength range of $1 < \lambda < 100$ µm. Since this L_{IR} is calculated from the fitted rest-frame component, no *k*-correction is needed. The values of $q_{\mathrm{IR}} = L_{\mathrm{IR}}/L_{150}$ are plotted as a function of redshift and radio power in Fig. 8, where the radio luminosities have been *k*-corrected assuming a spectral index of -0.7. As expected, below a redshift of ∼1, most of the sources lie on the FIR-radio correlation and their radio emission can be attributed to star formation alone. The opposite is true at higher redshifts, but there remain some sources near the FIR-radio correlation particularly in the lower radio power range of $10^{25} \gtrsim P_{150\,\mathrm{MHz}} \gtrsim 10^{26}$ W Hz^{-1}. We therefore consider galaxies with values within 2σ of the FIR-radio correlation as star-forming and exclude them from the subsequent RL AGN analysis. We use the FIR-radio correlation of Calistro Rivera et al. (2017), $q_{\mathrm{IR}} = 1.72(1 + z)^{-0.22}(\sigma = 0.529)$, which is based on LOFAR and *Herschel* measurements.

6.2 HERG/LERG separation

We aim to differentiate between HERGs (‘cold mode’ or ‘radiative mode’ sources), and LERGs (‘hot mode’ or ‘jet mode’ sources) based on their broad-band SED information. In the remainder of the paper, we use the nomenclature of HERGs and LERGs for succinctness. The AGNFITTER parameters of interest for our purposes are the disentangled host galaxy and AGN luminosities that together contribute to the emission at MIR wavelengths. The total MIR emission is the sum of the AGN torus luminosity $L_{\nu,\,\mathrm{TO}}$, as well as the stellar emission $L_{\nu,\,\mathrm{GA}}$ and the reprocessed cold/warm dust emission $L_{\nu,\,\mathrm{SB}}$. To allow for comparison, we define the integrated luminosities, L_{TO}, L_{GA}, L_{SB}, and L_{BB}, over the respective templates in a single rest-frame wavelength range of $1 < \lambda < 30$ µm. From these integrated luminosities, we calculate the value,

$$f_{\mathrm{AGN}} = \frac{L_{\mathrm{TO}} + L_{\mathrm{BB}}}{L_{\mathrm{TO}} + L_{\mathrm{GA}} + L_{\mathrm{BB}}}, \tag{4}$$

which quantifies the fraction of MIR emission that arises from an AGN compared with that from the stellar component of the host galaxy, *independent* of the MIR star-forming component. The MIR AGN emission we consider here mainly arises from the torus component, but we also include the BB component, which despite peaking at optical/uv wavelengths can be comparable to the GA component at these MIR wavelengths for strong, unobscured Type I AGN. We specifically do not consider in the denominator of this ratio the SB component, as this arises from the reprocessed cold/warm dust in star-forming galaxies and can dominate the MIR part of the SED in moderately strong AGN in star-forming galaxies. This allows us to identify AGN across a range in SFRs. Essentially the ratio of equation (4) is a measure of the strength of the MIR AGN emission compared to the stellar mass of the galaxy, traced by the GA component. The error of f_{AGN} is calculated by propagating the errors on L_{TO} and L_{GA} given by AGNFITTER. We expect that HERGs will have significant contribution to the IR emission from the torus (or obscuring structure) and thus have large f_{AGN} values,

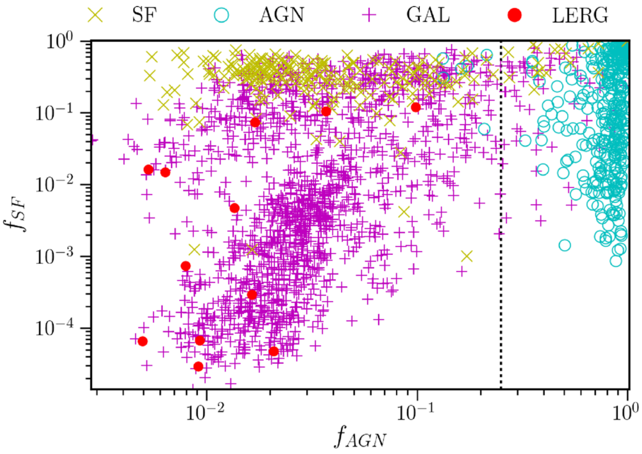

Figure 9. Torus and starburst emission fractions derived from the AGNFITTER SEDs for SDSS DR12 sources in the Boötes field showing the different SDSS spectral classes described in the text: optical AGN (cyan crosses), star-forming (SF; yellow crosses), and galaxies (GAL; magenta crosses). The large red points show the values for the Boötes field LERGs in the BH12 sample. The dotted vertical line shows the value of $f_{\mathrm{AGN}} = 0.25$ that we use to separate HERGs and LERGs.

while LERGs will have little or no such contribution and low f_{AGN} values. Similarly, we define the quantity

$$f_{\mathrm{SF}} = \frac{L_{\mathrm{SB}}}{L_{\mathrm{SB}} + L_{\mathrm{GA}}}, \tag{5}$$

to quantify the fraction of IR-emission due to star formation relative to that from the galaxy, independent of the AGN emission. The error of f_{SF} is calculated by propagating the errors on L_{SB} and L_{GA} given by AGNFITTER.

To investigate how these values correspond to classifications based on spectroscopy, we cross-matched sources in the full optical photometry catalogue with sources from the SDSS Data Release 12 spectroscopic sample (DR12; Alam et al. 2015), using a simple nearest neighbour match within 1 arcsec. This yielded a sample of 2315 sources for which we have an SDSS spectral classification and the same set of broad-band photometry used for the radio sources in this paper. As this is an SDSS-selected sample, it is restricted in redshift to $z < 0.3$. Using the spectroscopic redshifts[2] from SDSS, we fitted the broad-band SEDs in AGNFITTER. The resulting distribution of the derived f_{AGN} and f_{SF} values is shown in Fig. 9, separated by their SDSS spectral classification, which is based on the optical emission lines in the SDSS spectra (see Bolton et al. 2012). There is some overlap at intermediate values, but the respective populations generally occupy different regions. It is clear that most of the 387 sources classed as ‘AGN’ in SDSS DR12 (with spectral class either ‘QSO’ or ‘AGN’) have values of f_{AGN} close to one, indicating the presence of an excess of MIR emission from a torus as expected from these optical AGN. Similarly, the 217 sources identified as ‘star-forming’ (SDSS spectral class either ‘STARFORMING’, or ‘STARBURST’) have values of f_{SF} close to one. Finally, the 1711 remaining galaxies (SDSS spectral class ‘GALAXY’, i.e. those without any significant spectral lines) generally have small f_{AGN} and f_{SF} values, consistent with them being quiescent. The population of galaxies with large f_{SF} values could be explained by a lack of signal to noise in the spectral lines necessary to meet the requirements to be classified as star forming.

Since LERGs are expected to have no contribution from torus of accretion disc emission, we expect LERGs to have small values of f_{AGN}. We consider the radio sources from the $z < 0.3$ Best & Heckman (2012, hereafter BH12) sample, which are separated into HERGs and LERGs based on emission line diagnostics. Given the space density of sources in the BH12 catalogue, it is not unexpected that we find only LERGs within the ∼9 deg^2 Boötes field. All these LERGs have $f_{\mathrm{AGN}} \lesssim 0.1$. While there is no strict boundary separating these sources, four per cent of normal galaxies have $f_{\mathrm{AGN}} > 0.25$, and one per cent of optical AGN have $f_{\mathrm{AGN}} < 0.25$. Based on this, we define a separation of $f_{\mathrm{AGN}} = 0.25$ and in what follows we classify radio sources above this value as HERGs and below as LERGs. Finally, it should be noted that not all misclassifications are necessarily due to the faults of the SED fitting. It is possible that the spectral classifications here miss Type II obscured AGN.

We have further considered how this classification works for the 875 radio sources in the Boötes field for which we have optical spectra from AGES (Kochanek et al. 2012). The advantage of this test is that it probes sources fainter than the SDSS sample above. Similarly to the SDSS spectral classification, we use a BPT (Baldwin, Phillips & Terlevich 1981) classification for SF galaxies. While this limits the sample to $z < 0.35$ (366 sources) where the relevant emission lines lie within the AGES spectral coverage, it provides a clean separation between star-forming galaxies and AGN. We measured the strength and width of the H α, H β, [O III]λ5007 Å and [N II]λ6583 Å lines from the AGES spectra using routines in ASTROPY (Astropy Collaboration et al. 2013) to jointly fit the [N II]λ6548 Å–H α–[N II]λ6583 Å, H β, and [O III]λ4959 Å–[O III]λ5007 Å line profiles. We then used the separation

$$\log (\mathrm{O\,III}\ /\mathrm{H}\,\beta) < 0.61/\left[\log (\mathrm{N\,II}\ /\mathrm{H}\,\alpha) - 0.05\right] + 1.3$$

from Kauffmann et al. (2003) for sources with SNR >3 in all these lines to classify SF galaxies. The remaining sources are assumed to be RL AGN and are separated into HERGs and LERGs based on the strength and equivalent width of the [O III]λ5007 Å line (BH12; B14; Pracy et al. 2016). HERGs are taken to have SNR([O III]λ5007) > 3 and rest frame EW([O III]λ5007) > 5 Å. This AGES sample contains 141 SF galaxies, 197 LERGs, and 28 HERGs. Fig. 10 shows the distribution of the derived f_{AGN} and f_{SF} values for these sources. As for the SDSS sample, a similar trend is seen, in that the SF galaxies generally have f_{SF} close to one while HERGs have high f_{AGN} compared to the lower f_{AGN} values of LERGs. One per cent of LERGs have $f_{\mathrm{AGN}} > 0.25$, while 14 per cent of HERGs have $f_{\mathrm{AGN}} < 0.25$. It should be noted that the SF/LERG/HERG classification shown in this plot pertains only to the classification based on the optical spectra of these sources and as such the radio emission may be a result of either star formation or AGN activity, thus most of the sources with high f_{SF} values lie on the FIR-radio correlation (cf. Section 6.1).

Finally, we investigated a single cut in 22 µm flux separating LERGs and HERGs (Gürkan et al. 2014). Similar to Janssen et al. (in preparation), we find a large spread in 22 µm flux for both HERGs and LERGs classified either by their f_{AGN} values or their optical spectra. However, HERGs do generally have higher 22 µm fluxes than LERGs.

---

[2] Using our derived photometric redshifts for these sources instead of their SDSS spectroscopic redshifts in the AGNFITTER fits yields very similar results, and only increases the scatter slightly for this low redshift optically bright sample.

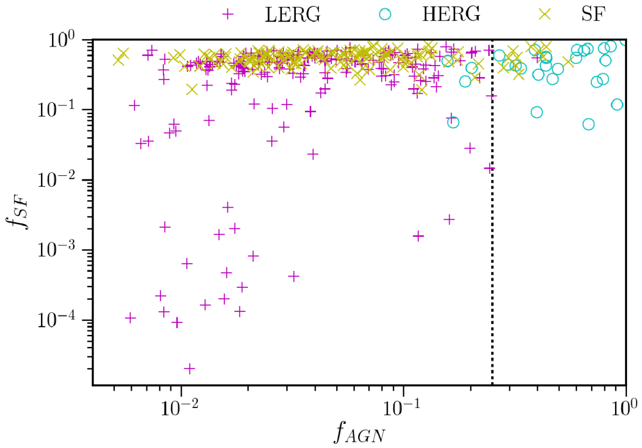

Figure 10. Torus and starburst emission fractions derived from the AGNFITTER SEDs for AGES sources in the Boötes field showing the different spectral classes: star-forming galaxies (SFGs; yellow crosses), HERGs (cyan crosses), and LERGs (magenta crosses). The dotted vertical line shows the value of $f_{\rm AGN} = 0.25$ that we use to separate HERGs and LERGs.

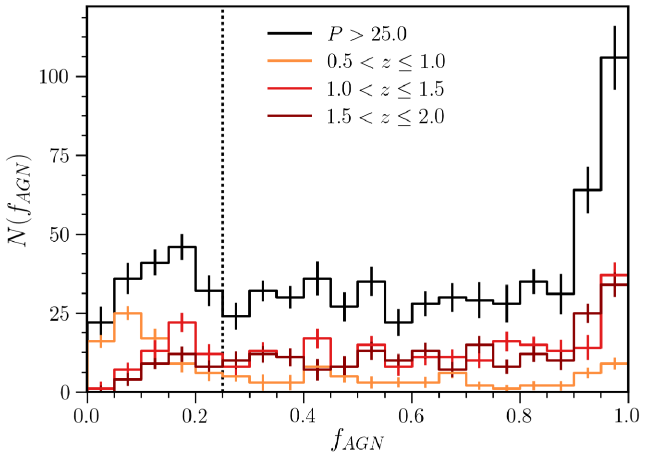

Figure 11. Distribution of the fraction of IR AGN emission, $f_{\rm AGN}$, defined by equation (4) for the full sample (black), and the three redshift intervals: $0.5 \leq z < 1.0$ (orange), $1.0 \leq z < 1.5$ (red), and $1.5 \leq z < 2.0$ (dark red). The dotted vertical line shows the value of $f_{\rm AGN} = 0.25$ that we use to separate HERGs and LERGs.

7 PROPERTIES OF RADIO SOURCES

7.1 Radio AGN at intermediate redshifts

The aim of this paper is to study the population of RL AGN at intermediate redshifts. The radio power-redshift plot (Fig. 4) shows that at low redshifts, $z \lesssim 0.3$, the radio-optical sample is dominated by low luminosity radio sources and contains very few high power sources, while at higher redshifts we can only probe high power sources. For this reason, we cannot use this sample to directly compare high luminosity sources at both low and high redshift. The wide LOFAR surveys will provide the areal coverage needed for such a comparison. The rms in the radio map varies across the field of view (see Williams et al. 2016) between 100 and 250 μJy beam^{-1}, meaning that at a given redshift the lowest power sources can only be detected over a smaller area. We do not make a cut on radio flux density, but account for incompleteness resulting from the varying detection area later (Sections 7.1.4 and 7.2). From the P–z plane, it is clear that there is increasing incompleteness above $z = 2$ and that at this redshift we can observe sources only with radio powers above $P_{150\,\rm MHz} \geq 10^{25}$ W Hz^{-1}. Therefore, to compare the same sources across redshifts in this section, we study only the high power ($P_{150\,\rm MHz} \geq 10^{25}$ W Hz^{-1}) sources at intermediate redshifts $0.5 \leq z < 2$. The final sample consists of 624 sources, which we divide into three redshift intervals:

(i) $0.5 \leq z < 1.0$ (134 sources),
(ii) $1.0 \leq z < 1.5$ (262 sources),
(iii) $1.5 \leq z < 2.0$ (228 sources).

These numbers reflect the number of sources in each bin based on their best photometric redshifts. We note that the final redshift bin may be incomplete below $P_{150\,\rm MHz} \lesssim 10^{25.5}$ W Hz^{-1}.

7.1.1 Local reference sample

As a local comparison sample, we use the catalogue compiled by BH12. This matched radio-optical catalogue was constructed from the seventh data release (DR7; Abazajian et al. 2009) of the Sloan Digital Sky Survey (SDSS) spectroscopic sample and the NRAO Very Large Array (VLA) Sky Survey (NVSS; Condon et al. 1998) and the Faint Images of the Radio Sky at Twenty centimetres (FIRST; Becker, White & Helfand 1995). The optical data includes parameters from the value-added spectroscopic catalogues (VASC) created by the Max Plank Institute for Astrophysics and Johns Hopkins University (MPA-JHU) group[3] (Brinchmann et al. 2004). This includes information from the imaging data such as magnitudes and sizes (York et al. 2000), as well as derived properties including the stellar mass based on fits to the photometry (Kauffmann et al. 2003). The spectroscopy also provides D_n4000 (Balogh et al. 1999) which, like galaxy colour, provides a guide to the stellar population age. BH12 separated the sources into star-forming galaxies and RL AGN (7302 sources), the latter of which are further sub-divided into HERGs and LERGs, based on their optical photometric and spectroscopic parameters. Noting the different observed radio frequency, we select sources with $P_{1.4\,\rm GHz} > 10^{24}$ W Hz^{-1}, broadly comparable to $P_{150\,\rm MHz} > 10^{25}$ W Hz^{-1}, assuming a spectral index of $\alpha = -0.7$. This local radio-optical sample consists of 3736 radio sources between $0.01 < z \leq 0.3$.

7.1.2 HERG/LERG composition

The distribution of $f_{\rm AGN}$ values for our intermediate redshift and high power, $P_{150\,\rm MHz} \geq 10^{25}$ W Hz^{-1}, samples is plotted in Fig. 11, where we show the distribution for all radio sources, and within each of the three redshift intervals. There is a maximum in the overall distribution for sources with $0.9 < f_{\rm AGN} < 1$, a second maximum for sources with $0.1 < f_{\rm AGN} < 0.2$, and a minimum around $f_{\rm AGN} \approx 0.5$. The two highest redshift intervals show the growing peak at $f_{\rm AGN} \approx 1$, which suggests that there are more 'strongly AGN-dominated' sources and fewer 'AGN-free' sources in these intervals than at $0.5 < z \leq 1.0$.

The number of HERGs and LERGs in each redshift interval are given in Table 1, including those for the local reference sample. The percentage of HERGs and LERGs within each redshift interval is given relative to the total number of radio sources in that interval. Here, we have considered the sources that lie on the FIR-radio correlation (see Section 6.1) as SF galaxies. It can be seen from these numbers that the fraction of HERGs rises between $z \approx 0$ and $0.5 \leq$

---

[3] Available at http://www.mpa-garching.mpg.de/SDSS/

Table 1. Number of SF, HERGs, and LERGs in the reference sample and the three redshift intervals.

z	N	SF (per cent)	HERGs (per cent)	LERGs (per cent)
0.01–0.3	3736	549 (15 per cent)	121 (4 per cent)	3066 (96 per cent)
0.5–1.0	134	11 (8 per cent)	50 (37 per cent)	73 (54 per cent)
1.0–1.5	262	71 (27 per cent)	153 (58 per cent)	38 (14 per cent)
1.5–2.0	228	117 (51 per cent)	94 (41 per cent)	17 (7 per cent)

$z < 1.0$, and then again between $0.5 \leq z < 1.0$ and $1.0 \leq z < 1.5$. The fraction of LERGs, on the other hand, is strongly declining between all redshift intervals. The spectroscopic completeness for both AGN types in the first redshift interval is ∼30 per cent, which for LERGs drops to below ∼2 per cent in the two higher redshift intervals, while for HERGs it only drops to ∼15 per cent.

7.1.3 Colour-mass distribution

We now consider the distribution of the RL AGN, both HERGs and LERGs, in colour-mass space. This is plotted in Fig. 12[4] for both optical and radio sources where we plot the $^{0.1}(u-r)$ colour (defined in Section 4.2) against stellar mass for both optical and radio sources in each of the four redshift intervals. The f_{AGN} values for the radio sources are colour-coded in the 2d distribution and the 1d distributions of both stellar mass and colour are shown for the optical and radio sources as well as separately for the HERGs and LERGs. Here, we use the value $f_{\mathrm{AGN}} = 0.25$ to separate the HERGs and LERGs. In comparing the local and higher redshift samples, we note that the parameters used for the HERG/LERG separation are different. However, they provide a qualitative comparison for the distribution of the radio and optical source populations in colour-mass space. Given the use of photometric parameters we expect there to be some fraction of catastrophic outliers. In particular, a few points at very high stellar masses, notably in the highest redshift bin, could be a result of poorly determined photometric redshifts and fitted masses.

The colour-mass distributions of optical and radio sources are clearly different, which is not unexpected. At all redshifts radio sources tend to be more massive and redder compared to the parent galaxy population. The properties of HERGs and LERGs are also different, in that the HERGs span a wider range of stellar masses $10^9 < M_*/\mathrm{M}_\odot < 10^{11.5}$ and colours. Going from the lower redshift bin, $0.5 \leq z < 1.0$, to the higher redshift bins, we see that the colour distribution of LERGs changes from showing a clear peak at $^{0.1}(u-r) > 2.5$, to becoming flatter where red and blue galaxies approximately contribute the same. Similarly for HERGs, we see an increasing contribution of very blue objects, $^{0.1}(u-r) < 0.1$, with redshift. In general, though, LERGs are always more likely to be hosted by massive red galaxies.

We compute the two sample Kolmorogorov-Smirnov two sided test statistics, and in all cases can reject the null hypothesis that the two samples are randomly drawn from the same distribution. The Kolmogorov-Smirnov statistics and p-values are given in Table 2. In the highest redshift bin in these plots, the radio source population is slightly incomplete due to the varying rms in the LOFAR map (see Section 7.1).

7.1.4 Radio-loud fraction

The mass dependence of the RL fraction can be an indicator of the accretion mode of the RL AGN, largely because of the different dependence of the fuelling source (hot versus cold gas) on stellar mass (Best et al. 2006) and the relationship between black hole and stellar mass for elliptical galaxies. As this is not a volume-limited sample, following Janssen et al. (2012) and Williams & Röttgering (2015), we use the RL fraction defined by

$$f_{\mathrm{RL}}^{y,x} = \left(\sum_{\mathrm{i}\in\mathrm{R}^{y,x}} \frac{1}{V_i^i}\right)\left(\sum_{\mathrm{j}\in\mathrm{A}^x} \frac{1}{V_i^j}\right)^{-1}, \qquad (6)$$

where the sets A and R are, respectively, all galaxies and all radio sources in a given bin, defined by the parameters of mass (x) and accretion mode (y) using the classification in Section 7.1.2 for radio sources. The maximum accessible volume over which each source can be observed, V_i, is determined by both the minimum and maximum distance at which a given source would be included in the sample as a result of the selection criteria: $V_i = V_{\max} - V_{\min}$, where $V_{\max}$ and $V_{\min}$ are the volumes enclosed within the observed sky area out to the maximum and minimum distances, respectively. The minimum accessible volume is a result of the lower redshift limit in a given bin. The maximum accessible volume is determined by the flux limits of the optical (<24 mag) and radio rms map as well as the upper limit of the redshift bin. Following Hardcastle et al. (2016), the radio $V_{\max}$ is calculated as $\int d_{\max}\mathrm{d}A$. The completeness function is determined from an rms map created by masking the LOFAR rms map by the optical coverage area, which excludes regions around bright optical sources. The total sky area of the masked map is 9.27 deg^2. For the optical, we use the rest-frame I-band magnitude determined from INTERREST to compute the $V_{\max}$. In order to take into account the uncertainties on the photometric redshifts, we consider the full photometric redshift PDFs from Duncan et al. (2017) in the calculation of the RL fractions. We do this by generating 100 realizations where the redshifts for each source are randomly drawn from their respective PDFs.[5] We compute for each realization the RL fraction described above. Uncertainties are calculated as the statistical Poissonian errors. We then take the median of the RL fraction realizations and the errors given are based on the 16th and 84th percentiles. This also takes into account which sources are included in each redshift interval.

The RL fraction for all radio sources and separately for HERGs and LERGs is shown in Fig. 13. It can be seen that the RL fraction for HERGs at all masses increases with redshift. It is possible the RL fraction in the highest redshift bin is slightly underestimated due to incompleteness between $10^{25} < P_{1.4\,\mathrm{GHz}} < 10^{25.5}$ W Hz^{-1} (cf. Section 7.1). The rising fraction of HERGs in massive galaxies becomes similar to the fraction of LERGs in the most massive galaxies at the highest redshifts. These results are consistent with those from many of the earlier radio surveys, which suggest that the most powerful radio galaxies ($P_{1.4\,\mathrm{GHz}} \gtrsim 10^{26}$ W Hz^{-1}) at $z \gtrsim 1$ are predominantly HERGs hosted by the most massive ($M_* \gtrsim 10^{12}\,\mathrm{M}_\odot$) galaxies (e.g. Eales et al. 1997; Jarvis et al. 2001; Seymour et al. 2007; Fernandes et al. 2015). The dependence on stellar mass is flatter for HERGs than it is for LERGs at all redshifts. Table 3 gives the value of the slope fitted to $\log f_{\mathrm{RL}}$–$\log(M_*/\mathrm{M}_\odot)$ over the range of $10^9 < M_*/\mathrm{M}_\odot < 10^{12}$. The shape of the RL fraction as a function

---

[4] A preliminary version of this figure was presented in Williams et al. (2015).

[5] For the sources with spectroscopic redshifts, we use a single sample at the spectroscopic redshift.

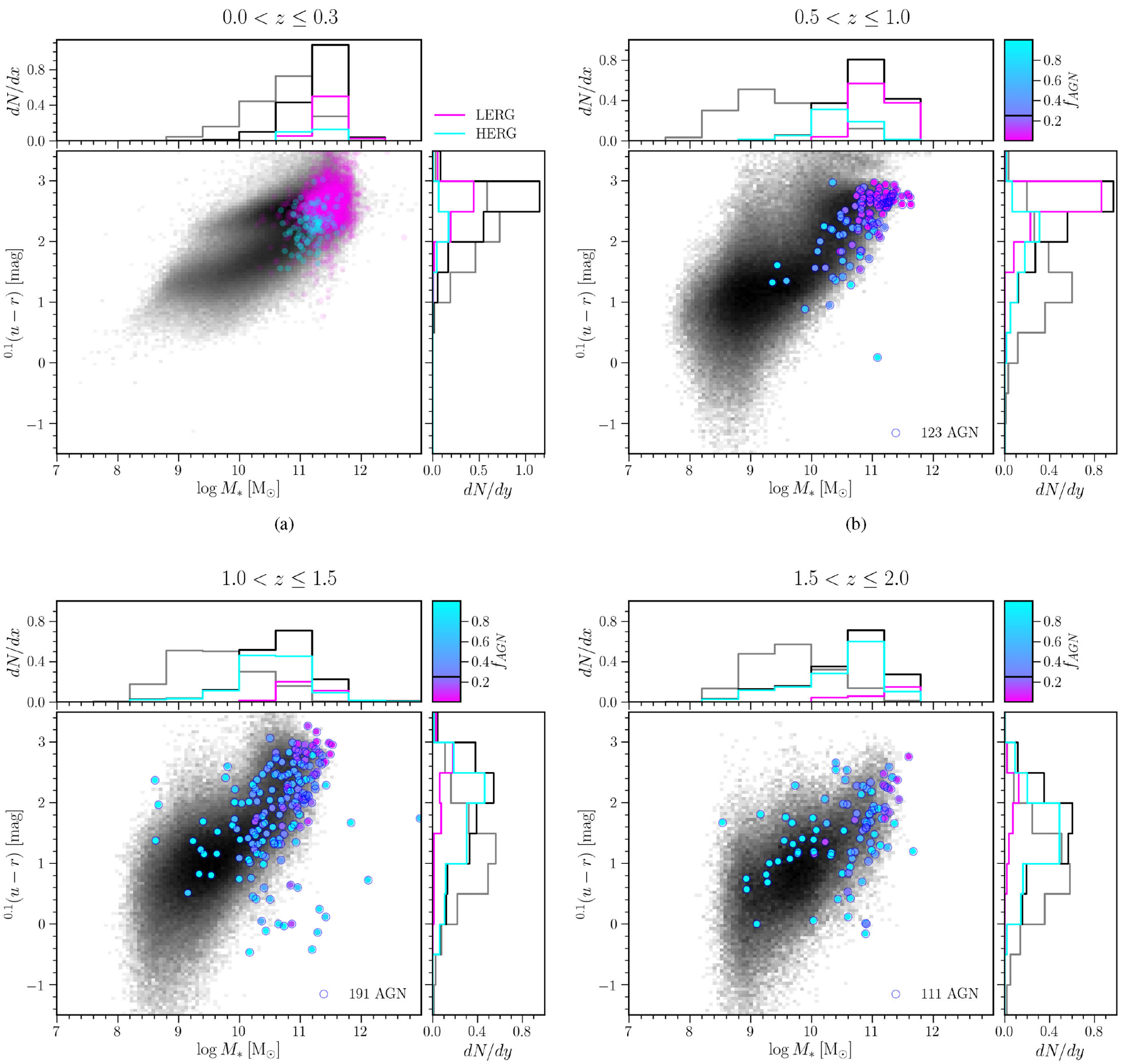

(a) (b) (c) (d)

Figure 12. Colour, $^{0.1}(u-r)$, versus stellar mass (*main* panels). The density of optical sources with $m_I < 24$ mag is plotted in black, in log units, and the radio sources are plotted in colour. The sub-panels show the normalized stellar mass (*top*) and colour distributions (*right*) for optical sources (grey) and radio sources (black). The HERG ($f_{\rm AGN} > 0.25$) and LERG ($f_{\rm AGN} < 0.25$) distributions are shown in cyan and magenta, respectively, normalized to the total number of radio sources. In the sub-panels, the HERG distributions are multiplied by a factor of 10 for visibility. Four redshift intervals are plotted separately: (a) the local BH12, $0.01 \leq z < 0.3$, spectroscopic sample where HERGs and LERGs are classified spectroscopically; (b–d) the three higher redshift samples from the Boötes field where the fill-colour of the radio points indicates their $f_{\rm AGN}$ values.

Table 2. Two-sided Kolmogorov–Smirnov (K-S) statistics in comparing the HERG and LERG distributions in colour and mass within each redshift interval.

z	$^{0.1}(u-r)$		$\log M_*/\mathrm{M}_\odot$	
	K-S statistic	p-value	K-S statistic	p-value
0.5–1.0	0.62	1.1×10^{-10}	0.57	4.3×10^{-9}
1.0–1.5	0.46	2.5×10^{-6}	0.48	9.6×10^{-7}
1.5–2.0	0.44	4.8×10^{-3}	0.61	2.3×10^{-5}

of stellar mass for LERGs remains almost the same steep function, $f_{\rm RL} \sim M_*^{2.0-2.5}$. This is very similar to that observed in the local Universe (Tasse et al. 2008b; Simpson et al. 2013). Importantly, this suggests that the fueling mechanism for LERGs remains the same out to redshifts of about 2, a prediction made by B14.

7.2 Luminosity functions for HERGs and LERGs

The LFs of the different radio AGN populations were first constructed by BH12. Since then, B14 have looked at the evolution

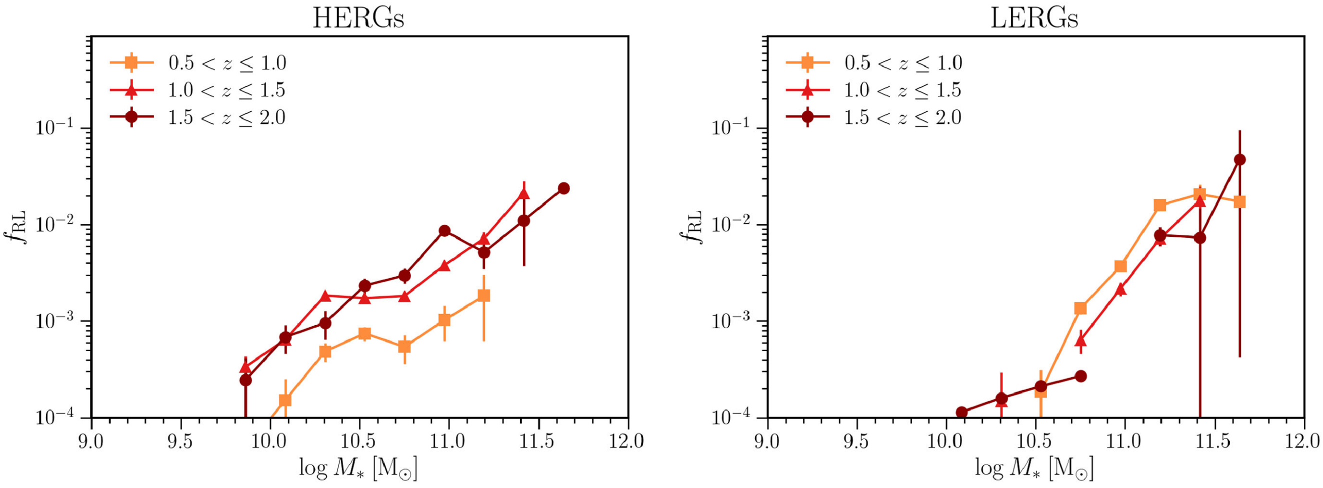

Figure 13. The fraction of galaxies hosting a radio source (RL fraction) as a function of stellar mass for a radio-power cut-off of $P_{150\,{\rm MHz}} > 10^{25}\,{\rm W\,Hz^{-1}}$ in the three redshift bins, for HERGS (left) and LERGs (right). The errors are determined from Poisson statistics.

Table 3. Slope of the RL fraction as a function of mass for HERGs and LERGs in the three redshift intervals.

z	HERGs	LERGs
0.5–1.0	0.55 ± 0.23	2.31 ± 0.29
1.0–1.5	0.67 ± 0.18	2.18 ± 0.13
1.5–2.0	1.17 ± 0.20	1.79 ± 0.33

of these LFs out to $z \sim 1$. Recently, Pracy et al. (2016) studied their evolution in finer detail using a much larger sample of over 5000 sources with spectroscopic redshifts and classifications, again covering the range of $0.005 < z < 0.75$. Within this redshift range LERGs show little evolution, explained by the very slow evolution of available massive elliptical host galaxies. However, these are predicted to drop off more strongly after $z > 1$ (see B14). In this paper, we probe this evolution out to $z \sim 2$, making use of photometric redshifts and the photometric AGN classification described in the previous section.

In order to take into account the uncertainties on the photometric redshifts, we consider the full photometric redshift PDFs from Duncan et al. (2017) in the calculation of the LFs, in a similar way to the RL fraction. We do this by generating 100 realizations of the LFs, where in each realization the redshifts for each source are randomly drawn from their respective PDFs.[6] We compute for each realization the individual radio LFs for the SF sources and the two populations of AGN in the standard way, using the $\rho = \Sigma_i 1/V_i$ formalism (Schmidt 1968; Condon 1989) where $V_{\rm max}$ is calculated the same way as in Section 7.1.4. Uncertainties are calculated as the statistical Poissonian errors. We then take the median of the LF realizations and the errors given based on the 16th and 84th percentiles. Given the large area covered, we assume that the effects of cosmic variance are negligible even for very massive galaxies.

The local LFs, split into AGN and SF categories, have been well studied at higher frequencies (Best et al. 2005a; Mauch & Sadler 2007; Prescott et al. 2016), and recently also with LOFAR (Hardcastle et al. 2016). Although not plotted here our SF and total AGN LFs show very good agreement with those of Hardcastle et al. (2016). The AGN LFs have been studied for the two accretion modes to a lesser extent only more recently (BH12; Pracy et al. 2016), with the reasons for the observed differences largely attributed to different selections and classification schemes (Pracy et al. 2016). Due to the relatively small areal coverage of the sample presented here, it is not very well suited to probing the AGN population in the local Universe; however, we have included the $0.01 < z < 0.3$ LFs for the various populations here (Fig. 14) as a comparison and as test of the ability of the photometric methods to separate the populations. For comparison, we show the LFs from Pracy et al. (2016) and BH12 and find our LFs to be broadly consistent with these.

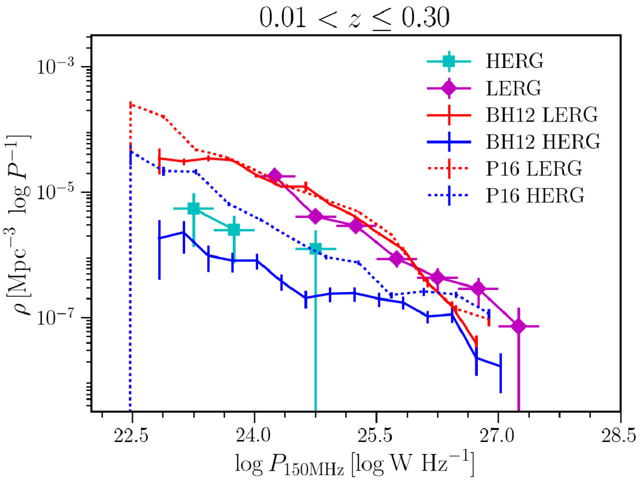

Figure 14. The radio LFs for the local, $0.01 < z < 0.3$, sample, separated into SF and AGN accretion modes. For comparison, the LFs of Pracy et al. (2016), labelled P16, and BH12, are included (both scaled from 1.4 GHz and to the same units).

At intermediate redshifts, we can probe the AGN LFs across a broad range in radio power, up to $P_{150\,{\rm MHz}} \approx 10^{28}\,{\rm W\,Hz^{-1}}$. The LFs for the RL AGN classified as HERGs and LERGs are shown in

---

[6] For the sources with spectroscopic redshifts, we use a single sample at the spectroscopic redshift.

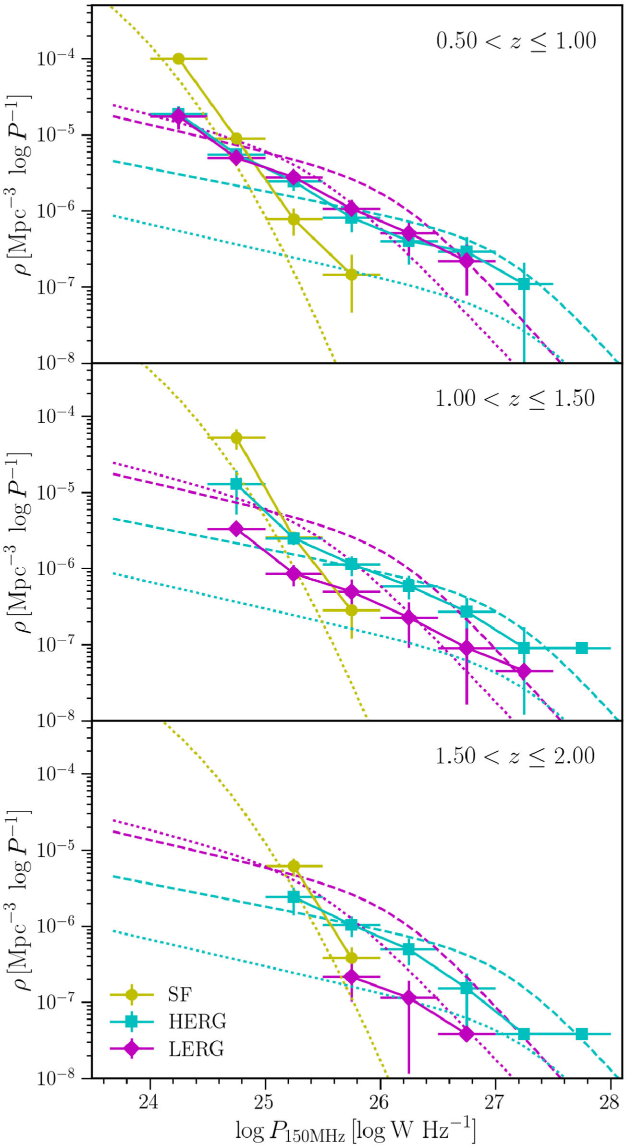

Figure 15. The radio LFs for our three intermediate redshift samples, separated into SF galaxies, HERGs and LERGs. For comparison and as a guide for the eye, the $z < 0.3$ (dotted) and $0.5 < z < 1.0$ (dashed) HERG and LERG LFs fitted by B14 are shown in all panels. We also show the simple model SF LFs from Novak et al. (2017) at each redshift interval.

Fig. 15 and tabulated in Table 4, for three redshift intervals $0.5 < z \leq 1.0$, $1.0 < z \leq 1.5$, and $1.5 < z \leq 2.0$. The SF LFs are also included. From these plots, it is clear that the HERG LFs show no statistically significant evolution across this redshift range – the LFs differ by less than 2σ. This is in contrast to the strong evolution seen between $z < 0.3$ and $0.5 < z < 1.0$ (B14). Despite the lack of evolution there is a suggestion that at the high power end ($P_{150\,\mathrm{MHz}} \gtrsim 10^{26}\,\mathrm{W\,Hz^{-1}}$) the space density peaks in the second redshift interval $1.0 < z \leq 1.5$. This is only marginally significant as the space density above $P_{150\,\mathrm{MHz}} > 10^{26}\,\mathrm{W\,Hz^{-1}}$ in the second interval is only $\sim 2\sigma$ above that in the first interval and $\sim 1.5\sigma$ above that in the third interval. Nevertheless, it is consistent with what is known about the space density evolution of the RL AGN population as a whole. The space density of the highest power ($P_{1.4\,\mathrm{GHz}} \gtrsim 10^{25}\,\mathrm{W\,Hz^{-1}}$) radio sources is well known to peak at $z \approx 1$ (Dunlop & Peacock 1990; Rigby et al. 2011, 2015).

In contrast, the space density of LERGs is strongly declining significantly. The evolution of the LERG population is of particular interest. In Fig. 16, we plot only the LERG LFs along with the models of B14 at the relevant redshifts. These are models fitted to the LERG LFs out to $z < 1$. For more details of these models, we refer the reader to B14 and mention here the key points. The 'model 1' models are for pure density evolution, where the evolution of LERGs is driven purely by the strongly declining population of quiescent galaxies, with a possible time lag between the formation of a quiescent galaxy and the onset of radio activity (variant *b*). The 'model 2' models are similar but include a luminosity evolution of the sources, i.e. the luminosities of the radio sources systematically increase with redshift. The third type of model, 'model 3' includes a contribution of HERG-type sources. The LERG LFs do suggest the 'model 2a' or 'model 2b' are preferred over some of the other models.

8 CONCLUSION

We have presented a catalogue of radio sources from the 150-MHz LOFAR observations of the Boötes field (Williams et al. 2016) matched to optical sources from the multi-band photometry catalogue (Brown et al. 2007) available for the Boötes field, which have photometric redshifts from Duncan et al. (2017). We have performed SED fitting using AGNFITTER (Calistro Rivera et al. 2016), including the FIR flux measurements, to ascertain the relative contribution of AGN and galaxy emission in the MIR ($1 < \lambda < 30\,\mu\mathrm{m}$) and used this to classify radio galaxies as HERGs or LERGs. We have used a well-defined sub-sample of 624 high-power ($P_{150\,\mathrm{MHz}} > 10^{25}\,\mathrm{W\,Hz^{-1}}$) radio sources with redshifts between $0.5 \leq z < 2$ to study the RL fraction as a function of galaxy mass. We have derived the radio LFs separately for HERGs and LERGs. Our key findings can be summarized as the following:

(i) The fraction of HERGs is significantly higher at $z = 2$ compared to $z = 0$.

(ii) LERGs are generally found in passive galaxies, while the host galaxies of HERGs are both star forming and passive.

(iii) LERGs tend to be hosted by more massive galaxies than HERGs and are predominantly found in redder galaxies, but at higher redshifts can also be found in bluer galaxies.

(iv) The fraction of galaxies hosting LERGs is a strong function of stellar mass like it is in the local Universe, suggesting these sources are still fuelled by accretion of hot gas.

(v) At moderate redshifts, $0.5 < z < 2.0$, the LF of LERGs undergoes strong negative evolution consistent with the decline of quiescent galaxies in the Universe.

While we have used the full photometric redshift PDFs to take into account the uncertainties on their estimates, this kind of panchromatic SED decomposition would benefit greatly from spectroscopic redshifts, in particular for the sources with broad photometric redshift distributions. We have used a local comparison sample at low redshift, there is no directly comparable sample to track the evolution from $z \approx 0$. In the near future, the full LOFAR surveys (Shimwell et al. 2017), both wide and deep, combined with spectroscopic information from WEAVE-LOFAR (Smith et al. 2016), providing both redshifts and spectral classification, will allow us to address both these issues and will allow this to be done with greater accuracy and in more detail for larger samples.

Table 4. Radio LFs in three redshift intervals separated by SF and AGN types.

	All		SF		LERGs		HERGs	
log P_{150} W Hz^{-1}	N	log ρ (Mpc^{-3} log P^{-1})	N	log ρ (Mpc^{-3} log P^{-1})	N	log ρ (Mpc^{-3} log P^{-1})	N	log ρ (Mpc^{-3} log P^{-1})
$0.50 < z \leq 1.00$								
24.25	299	$-3.86^{+0.05}_{-0.05}$	200	$-4.00^{+0.06}_{-0.07}$	49	$-4.76^{+0.14}_{-0.14}$	48	$-4.73^{+0.12}_{-0.14}$
24.75	249	$-4.71^{+0.03}_{-0.04}$	112	$-5.04^{+0.05}_{-0.05}$	67	$-5.31^{+0.06}_{-0.06}$	70	$-5.26^{+0.07}_{-0.09}$
25.25	82	$-5.22^{+0.06}_{-0.06}$	10	$-6.11^{+0.18}_{-0.17}$	38	$-5.56^{+0.08}_{-0.09}$	32	$-5.61^{+0.09}_{-0.11}$
25.75	27	$-5.71^{+0.10}_{-0.11}$	2	$-6.84^{+0.36}_{-0.30}$	14	$-5.97^{+0.14}_{-0.13}$	11	$-6.09^{+0.16}_{-0.16}$
26.25	13	$-6.02^{+0.14}_{-0.16}$	...	...	7	$-6.29^{+0.18}_{-0.21}$	6	$-6.40^{+0.22}_{-0.22}$
26.75	7	$-6.29^{+0.20}_{-0.17}$	...	...	3	$-6.66^{+0.28}_{-0.28}$	4	$-6.54^{+0.25}_{-0.24}$
27.25	2	$-6.84^{+0.38}_{-0.38}$	...	...	...	...	2	$-6.96^{+0.40}_{-0.40}$
27.75	...	...	...	...	...	...	...	...
$1.00 < z \leq 1.50$								
24.25	...	...	...	...	...	...	...	...
24.75	175	$-4.15^{+0.11}_{-0.11}$	111	$-4.28^{+0.12}_{-0.13}$	18	$-5.48^{+0.38}_{-0.62}$	45	$-4.89^{+0.22}_{-0.26}$
25.25	135	$-5.23^{+0.05}_{-0.05}$	59	$-5.59^{+0.07}_{-0.07}$	19	$-6.07^{+0.13}_{-0.14}$	55	$-5.60^{+0.08}_{-0.08}$
25.75	42	$-5.71^{+0.09}_{-0.10}$	6	$-6.55^{+0.23}_{-0.25}$	10	$-6.30^{+0.20}_{-0.18}$	24	$-5.94^{+0.12}_{-0.14}$
26.25	18	$-6.09^{+0.13}_{-0.13}$	...	...	5	$-6.65^{+0.26}_{-0.26}$	13	$-6.23^{+0.16}_{-0.14}$
26.75	7	$-6.50^{+0.18}_{-0.21}$	...	...	2	$-7.04^{+0.36}_{-0.36}$	6	$-6.57^{+0.23}_{-0.19}$
27.25	3	$-6.87^{+0.37}_{-0.27}$	...	...	1	$-7.34^{+0.50}_{-0.66}$	2	$-7.04^{+0.38}_{-0.38}$
27.75	2	$-7.04^{+0.47}_{-0.49}$	...	...	...	...	2	$-7.04^{+0.48}_{-0.51}$
$1.50 < z \leq 2.00$								
24.25	...	...	...	...	...	...	...	...
24.75	...	...	...	...	...	...	...	...
25.25	98	$-5.04^{+0.09}_{-0.10}$	60	$-5.21^{+0.12}_{-0.12}$	...	...	33	$-5.62^{+0.15}_{-0.19}$
25.75	43	$-5.78^{+0.09}_{-0.10}$	10	$-6.42^{+0.17}_{-0.18}$	6	$-6.67^{+0.23}_{-0.23}$	27	$-5.98^{+0.12}_{-0.13}$
26.25	15	$-6.21^{+0.15}_{-0.14}$	...	...	3	$-6.94^{+0.30}_{-0.39}$	12	$-6.31^{+0.18}_{-0.17}$
26.75	5	$-6.72^{+0.26}_{-0.26}$	...	...	1	$-7.42^{+0.48}_{-0.65}$	4	$-6.82^{+0.25}_{-0.31}$
27.25	1	$-7.42^{+0.55}_{-0.70}$	...	...	...	...	1	$-7.42^{+0.50}_{-0.66}$
27.75	1	$-7.42^{+0.54}_{-0.69}$	...	...	...	...	1	$-7.42^{+0.52}_{-0.68}$

ACKNOWLEDGEMENTS

W.L.W. and M.J.H. acknowledge support from the UK Science and Technology Facilities Council [ST/M001008/1]. H.J.R. and K.J.D. gratefully acknowledge support from the European Research Council under the European Union's Seventh Framework Programme (FP/2007-2013)/ERC Advanced Grant NEW-CLUSTERS-321271. P.N.B. is grateful for support from the UK STFC via grant ST/M001229/1. G.J.W. gratefully acknowledges support from The Leverhulme Trust. M.J.J. acknowledges support from UK Science and Technology Facilities Council and the South African SKA Project. E.K.M. acknowledges support from the Australian Research Council Centre of Excellence for All-sky Astrophysics (CAASTRO), through project number CE110001020.

The authors thank C. S. Kochanek for access to the AGES spectra.

This research has made use of data from HerMES project, http://hermes.sussex.ac.uk/. HerMES is a *Herschel* Key Programme utilizing Guaranteed Time from the SPIRE instrument team, ESAC scientists and a mission scientist. *Herschel* is an ESA space observatory with science instruments provided by European-led Principal Investigator consortia and with important participation from NASA. The HerMES data were accessed through the *Herschel* Database in Marseille (HeDaM; http://hedam.lam.fr) operated by CeSAM and hosted by the Laboratoire d'Astrophysique de Marseille. The *Herschel* Extragalactic Legacy Project (HELP; Vaccari 2016) is bringing together all publicly available multiwavelength data sets within the regions of the sky observed in extragalactic *Herschel* surveys.

LOFAR, the Low Frequency Array designed and constructed by ASTRON, has facilities in several countries, that are owned by various parties (each with their own funding sources), and that are collectively operated by the International LOFAR Telescope (ILT) foundation under a joint scientific policy.

This research has made use of the University of Hertfordshire high-performance computing facility http://stri-cluster.herts.ac.uk/ and the LOFAR-UK computing facility located at the University of Hertfordshire and supported by STFC [ST/P000096/1]. This research made use of ASTROPY, a community-developed core PYTHON package for astronomy (Astropy Collaboration et al. 2013) hosted at http://www.astropy.org/, of APLPY, an open-source astronomical plotting package for PYTHON hosted at http://aplpy.github.com/, and of TOPCAT (Taylor 2005).

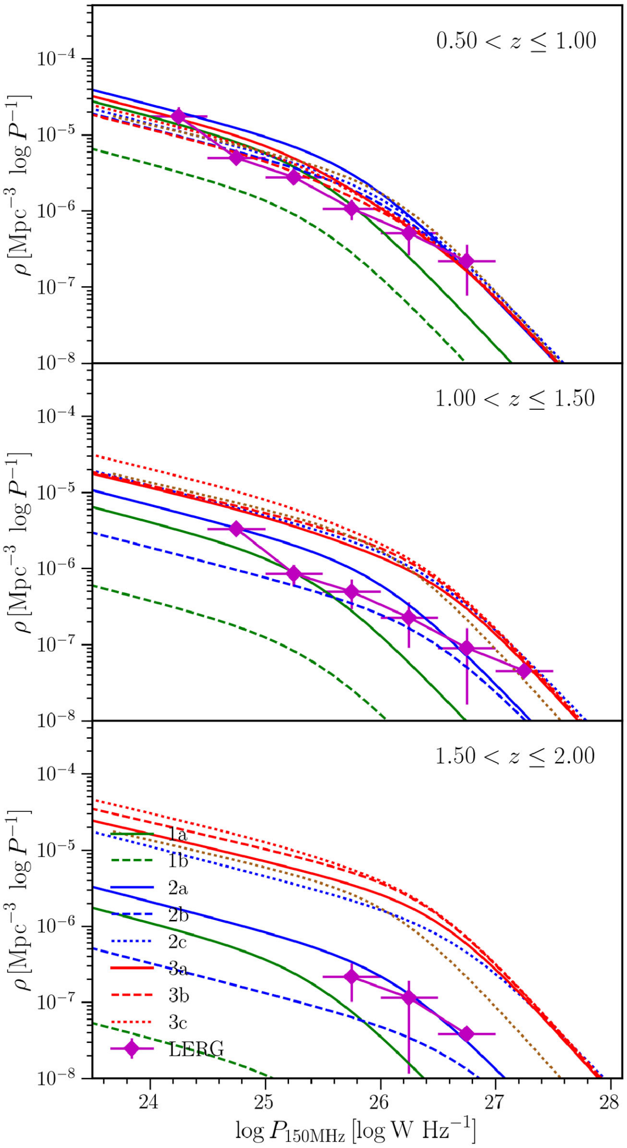

Figure 16. The LERG LFs for our three intermediate redshift samples.The models from B14 are shown in all panels.

REFERENCES

Abazajian K. N. et al., 2009, ApJS, 182, 543
Alam S. et al., 2015, ApJS, 219, 12
Almosallam I. A., Lindsay S. N., Jarvis M. J., Roberts S. J., 2016a, MNRAS, 455, 2387
Almosallam I. A., Jarvis M. J., Roberts S. J., 2016b, MNRAS, 462, 726
Antonucci R., 1993, ARA&A, 31, 473
Ashby M. L. N. et al., 2009, ApJ, 701, 428
Assef R. J. et al., 2010, ApJ, 713, 970
Astropy Collaboration et al., 2013, A&A, 558, A33
Baldwin J. A., Phillips M. M., Terlevich R., 1981, PASP, 93, 5
Balogh M. L., Morris S. L., Yee H. K. C., Carlberg R. G., Ellingson E., 1999, ApJ, 527, 54
Barthel P. D., 1989, ApJ, 336, 606
Becker R. H., White R. L., Helfand D. J., 1995, ApJ, 450, 559
Benn C. R., 1983, The Observatory, 103, 150
Bertin E., Arnouts S., 1996, A&AS, 117, 393
Best P. N., Heckman T. M., 2012, MNRAS, 421, 1569 (BH12)
Best P. N., Arts J. N., Röttgering H. J. A., Rengelink R., Brookes M. H., Wall J., 2003, MNRAS, 346, 627
Best P. N., Kauffmann G., Heckman T. M., Ivezić Ž., 2005a, MNRAS, 362, 9
Best P. N., Kauffmann G., Heckman T. M., Brinchmann J., Charlot S., Ivezić Ž., White S. D. M., 2005b, MNRAS, 362, 25
Best P. N., Kaiser C. R., Heckman T. M., Kauffmann G., 2006, MNRAS, 368, L67
Best P. N., von der Linden A., Kauffmann G., Heckman T. M., Kaiser C. R., 2007, MNRAS, 379, 894
Best P. N., Ker L. M., Simpson C., Rigby E. E., Sabater J., 2014, MNRAS, 445, 955 (B14)
Blanton M. R. et al., 2003a, AJ, 125, 2348
Blanton M. R. et al., 2003b, ApJ, 592, 819
Blanton M. R. et al., 2003c, ApJ, 594, 186
Bolton A. S. et al., 2012, AJ, 144, 144
Bower R. G., Benson A. J., Malbon R., Helly J. C., Frenk C. S., Baugh C. M., Cole S., Lacey C. G., 2006, MNRAS, 370, 645
Brammer G. B., van Dokkum P. G., Coppi P., 2008, ApJ, 686, 1503
Brinchmann J., Charlot S., White S. D. M., Tremonti C., Kauffmann G., Heckman T., Brinkmann J., 2004, MNRAS, 351, 1151
Brodwin M. et al., 2006, ApJ, 651, 791
Brown M. J. I., Dey A., Jannuzi B. T., Brand K., Benson A. J., Brodwin M., Croton D. J., Eisenhardt P. R., 2007, ApJ, 654, 858
Brown M. J. I. et al., 2008, ApJ, 682, 937
Brown M. J. I. et al., 2014, ApJS, 212, 18
Bruzual G., Charlot S., 2003, MNRAS, 344, 1000
Calistro Rivera G., Lusso E., Hennawi J. F., Hogg D. W., 2016, ApJ, 833, 98
Calistro Rivera G. et al., 2017, MNRAS, 469, 3468
Calzetti D., Armus L., Bohlin R. C., Kinney A. L., Koornneef J., Storchi-Bergmann T., 2000, ApJ, 533, 682
Cattaneo A. et al., 2009, Nature, 460, 213
Chabrier G., 2003, PASP, 115, 763
Chary R., Elbaz D., 2001, ApJ, 556, 562
Condon J. J., 1989, ApJ, 338, 13
Condon J. J., 1992, ARA&A, 30, 575
Condon J. J., Cotton W. D., Greisen E. W., Yin Q. F., Perley R. A., Taylor G. B., Broderick J. J., 1998, AJ, 115, 1693
Cool R. J. et al., 2012, ApJ, 748, 10
Croton D. J. et al., 2006, MNRAS, 365, 11
de Vries W. H., Morganti R., Röttgering H. J. A., Vermeulen R., van Breugel W., Rengelink R., Jarvis M. J., 2002, AJ, 123, 1784
Dahlen T. et al., 2013, ApJ, 775, 93
Dale D. A., Helou G., 2002, ApJ, 576, 159
Donley J. L. et al., 2012, ApJ, 748, 142
Duncan K. J., Jarvis M. J., Brown M. J. I., Rottgering H. J. A., 2017, MNRAS, preprint (arXiv:1712.04476)
Duncan K. J. et al., 2018, MNRAS, 473, 2655
Dunlop J. S., Peacock J. A., 1990, MNRAS, 247, 19
Eales S., Rawlings S., Law-Green D., Cotter G., Lacy M., 1997, MNRAS, 291, 593
Evans D. A., Worrall D. M., Hardcastle M. J., Kraft R. P., Birkinshaw M., 2006, ApJ, 642, 96
Fabian A. C., Celotti A., Erlund M. C., 2006, MNRAS, 373, L16
Fabricant D. et al., 2005, PASP, 117, 1411
Fanaroff B. L., Riley J. M., 1974, MNRAS, 167, 31P
Fernandes C. A. C. et al., 2015, MNRAS, 447, 1184
Griffin M. J. et al., 2010, A&A, 518, L3
Gürkan G., Hardcastle M. J., Jarvis M. J., 2014, MNRAS, 438, 1149
Hardcastle M. J., Evans D. A., Croston J. H., 2006, MNRAS, 370, 1893
Hardcastle M. J., Evans D. A., Croston J. H., 2007, MNRAS, 376, 1849
Hardcastle M. J. et al., 2013, MNRAS, 429, 2407
Hardcastle M. J. et al., 2016, MNRAS, 462, 1910
Heckman T. M., Best P. N., 2014, ARA&A, 52, 589
Hickox R. C. et al., 2009, ApJ, 696, 891
Hine R. G., Longair M. S., 1979, MNRAS, 188, 111

Ilbert O. et al., 2009, ApJ, 690, 1236

Jackson N., Rawlings S., 1997, MNRAS, 286, 241

Jannuzi B. T., Dey A., NDWFS Team, 1999, American Astronomical Society Meeting Abstracts. p. 1392

Jannuzi B. et al., 2010, American Astronomical Society Meeting Abstracts #215. p. 470.01

Janssen R. M. J., Röttgering H. J. A., Best P. N., Brinchmann J., 2012, A&A, 541, A62

Jarvis M. J. et al., 2001, MNRAS, 326, 1563

Kauffmann G. et al., 2003, MNRAS, 341, 33

Kochanek C. S. et al., 2012, ApJS, 200, 8

Kriek M., van Dokkum P. G., Labbé I., Franx M., Illingworth G. D., Marchesini D., Quadri R. F., 2009, ApJ, 700, 221

Laing R. A., Jenkins C. R., Wall J. V., Unger S. W., 1994, in Bicknell G. V., Dopita M. A., Quinn P. J., eds, ASP Conf. Ser. Vol. 54, The Physics of Active Galaxies. Astron. Soc. Pac., San Francisco, p. 201

Levenson L. et al., 2010, MNRAS, 409, 83

Magorrian J. et al., 1998, AJ, 115, 2285

Mauch T., Sadler E. M., 2007, MNRAS, 375, 931

McNamara B. R., Nulsen P. E. J., 2012, New J. Phys., 14, 055023

Mingo B., Hardcastle M. J., Croston J. H., Dicken D., Evans D. A., Morganti R., Tadhunter C., 2014, MNRAS, 440, 269

Muzzin A. et al., 2013, ApJS, 206, 8

Narayan R., Yi I., 1995, ApJ, 452, 710

Novak M. et al., 2017, A&A, 602, A5

Ogle P., Whysong D., Antonucci R., 2006, ApJ, 647, 161

Oliver S. J. et al., 2012, MNRAS, 424, 1614

Pracy M. B. et al., 2016, MNRAS, 460, 2

Prescott M. et al., 2016, MNRAS, 457, 730

Prestage R. M., Peacock J. A., 1983, MNRAS, 204, 355

Richter G. A., 1975, Astron. Nachr., 296, 65

Rigby E. E., Best P. N., Brookes M. H., Peacock J. A., Dunlop J. S., Röttgering H. J. A., Wall J. V., Ker L., 2011, MNRAS, 416, 1900

Rigby E. E., Argyle J., Best P. N., Rosario D., Röttgering H. J. A., 2015, A&A, 581, A96

Rowan-Robinson M. et al., 2008, MNRAS, 386, 697

Russell H. R., McNamara B. R., Edge A. C., Hogan M. T., Main R. A., Vantyghem A. N., 2013, MNRAS, 432, 530

Salvato M. et al., 2008, ApJ, 690, 1250

Salvato M. et al., 2009, ApJ, 690, 1250

Salvato M. et al., 2011, ApJ, 742, 61

Schmidt M., 1968, ApJ, 151, 393

Seymour N. et al., 2007, ApJS, 171, 353

Shakura N. I., Sunyaev R. A., 1973, A&A, 24, 337

Shimwell T. W. et al., 2017, A&A, 598, A104

Silk J., Rees M. J., 1998, A&A, 331, L1

Silva L., Maiolino R., Granato G. L., 2004, MNRAS, 355, 973

Simpson C., Westoby P., Arumugam V., Ivison R., Hartley W., Almaini O., 2013, MNRAS, 433, 2647

Smith D. J. B. et al., 2016, in Reylé C., Richard J., Cambrésy L., Deleuil M., Pécontal E., Tresse L., Vauglin I., eds, SF2A-2016: Proceedings of the Annual meeting of the French Society of Astronomy and Astrophysics. p. 271

Son D., Woo J.-H., Kim S. C., Fu H., Kawakatu N., Bennert V. N., Nagao T., Park D., 2012, ApJ, 757, 140

Stern D. et al., 2005, ApJ, 631, 163

Stern D. et al., 2012, ApJ, 753, 30

Sutherland W., Saunders W., 1992, MNRAS, 259, 413

Tasse C., Le Borgne D., Röttgering H., Best P. N., Pierre M., Rocca-Volmerange B., 2008a, A&A, 490, 879

Tasse C., Best P. N., Röttgering H., Le Borgne D., 2008b, A&A, 490, 893

Taylor M. B., 2005, in Shopbell P., Britton M., Ebert R., eds, ASP Conf. Ser. Vol. 347, Astronomical Data Analysis Software and Systems XIV. Astron. Soc. Pac., San Francisco, p. 29

Taylor E. N. et al., 2009, ApJS, 183, 295

Urry C. M., Padovani P., 1995, PASP, 107, 803

van Haarlem M. P. et al., 2013, A&A, 556, A2

van Weeren R. J. et al., 2016, ApJS, 223, 2

Vaccari M., 2016, Astrophys. Space Sci. Proc. Vol. 42, The Universe of Digital Sky Surveys. Springer International Publishing, Switzerland, p. 71

Whysong D., Antonucci R., 2004, ApJ, 602, 116

Williams W. L., Röttgering H. J. A., 2015, MNRAS, 450, 1538

Williams W., Rottgering H. J. A., Van Weeren R., Calistro Rivera G., 2015, Proc. Sci., Feeding the monsters at low frequencies: LOFAR & the evolution of radio-loud AGN. SISSA, Trieste, PoS(EXTRA-RADSUR2015)025

Williams W. L. et al., 2016, MNRAS, 460, 2385

Wilman R. J. et al., 2008, MNRAS, 388, 1335

Wolstencroft R. D., Savage A., Clowes R. G., MacGillivray H. T., Leggett S. K., Kalafi M., 1986, MNRAS, 223, 279

York D. G. et al., 2000, AJ, 120, 1579

APPENDIX A: RADIO-OPTICAL MATCHES

Some examples of the Class 1 and 2 sources with LR-matched optical sources are shown in Figs A1 and A2, respectively.

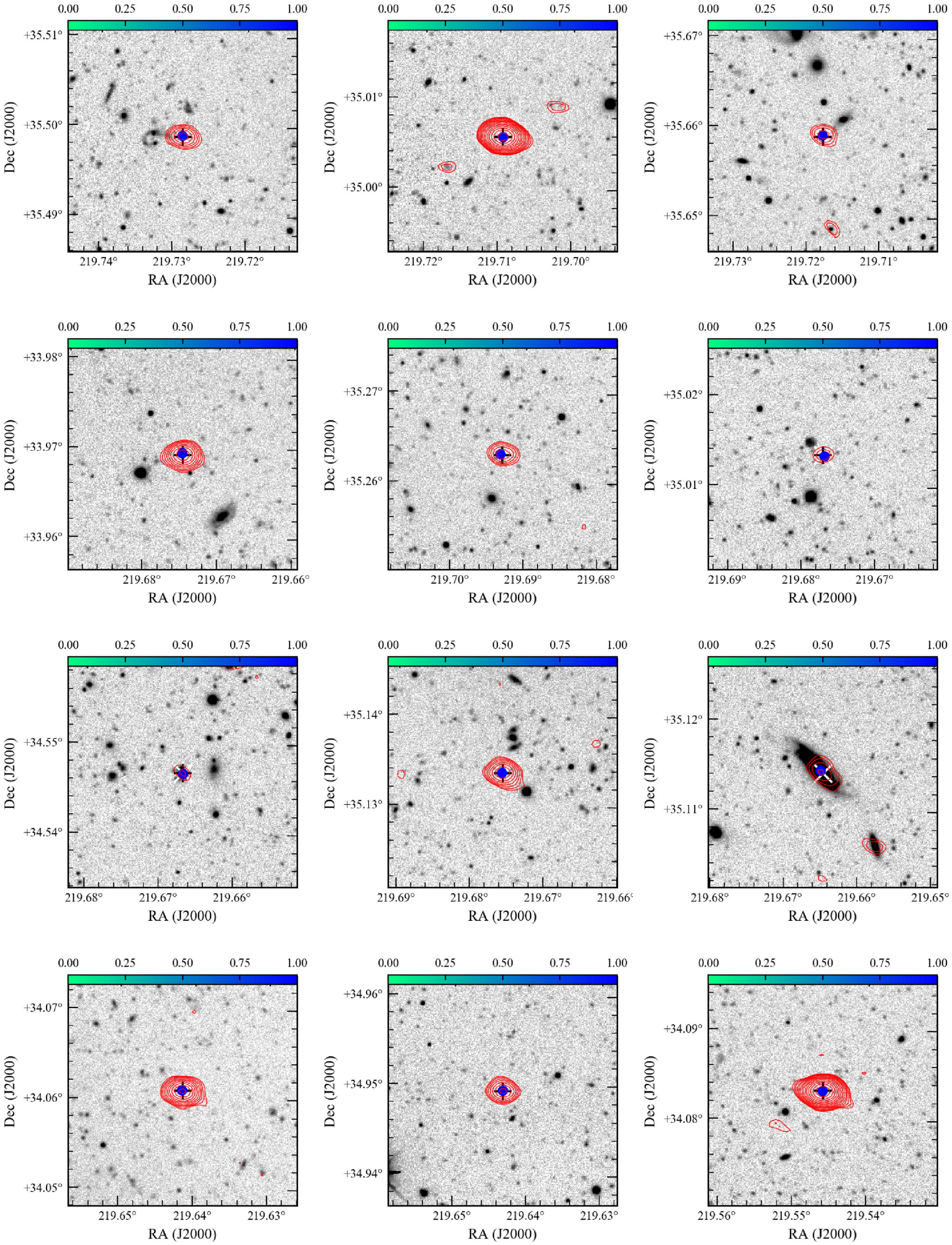

Figure A1. Examples of the radio-optical cross-matches in Class 1. The grey-scale image show the *I*-band NDWFS image. The red contours show the LOFAR 150-MHz image at levels of $3\sigma_{\mathrm{local}} \times [1, 1.4, 2, 2.8, \dots]$, where σ_{local} is the local rms in the LOFAR map at the source position. The black cross/white plus symbols show the flux-weighted radio position. The blue colour scale shows the LR probability of the matched optical source. Each image is 1.25 arcmin in diameter.

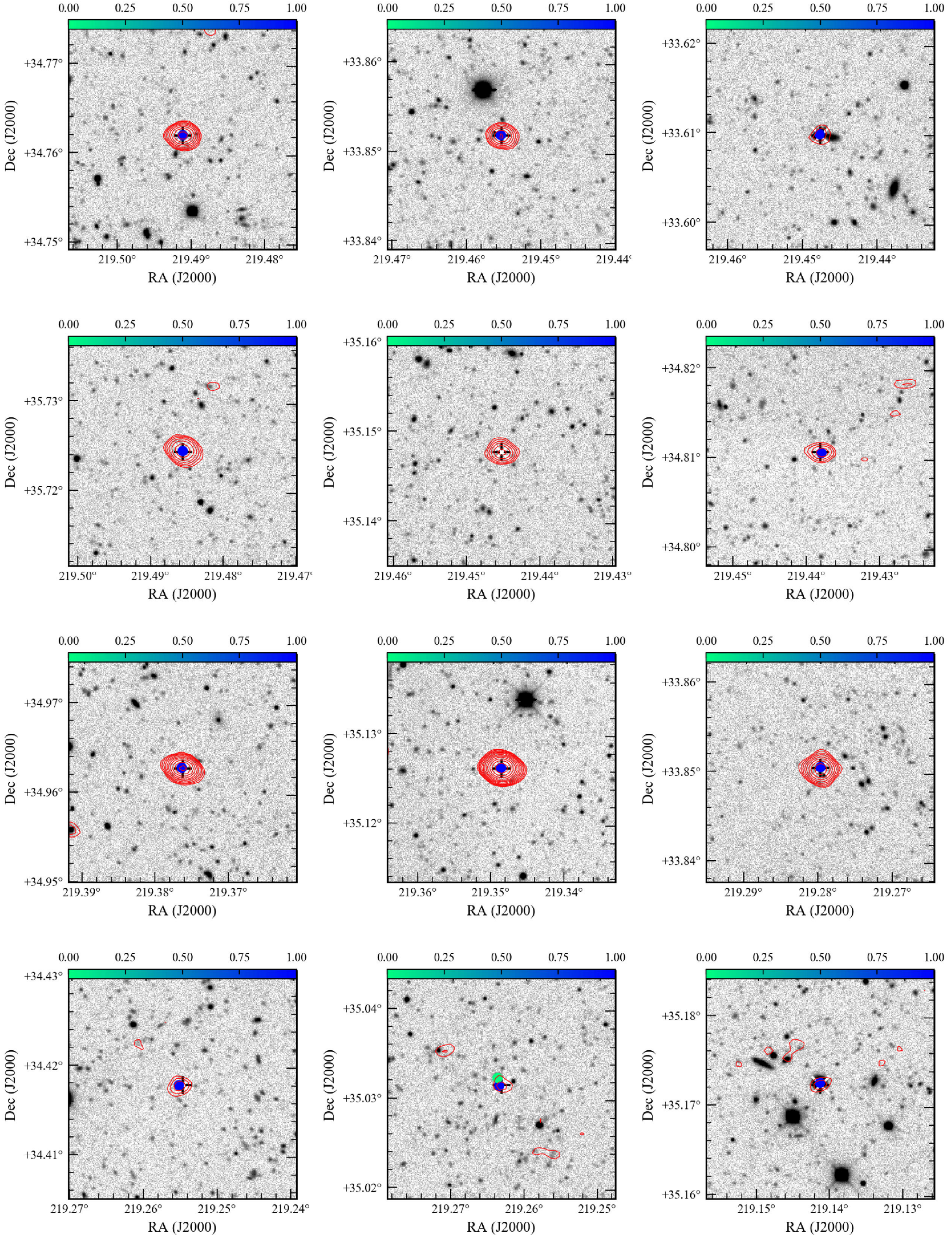

Figure A1 – *continued*

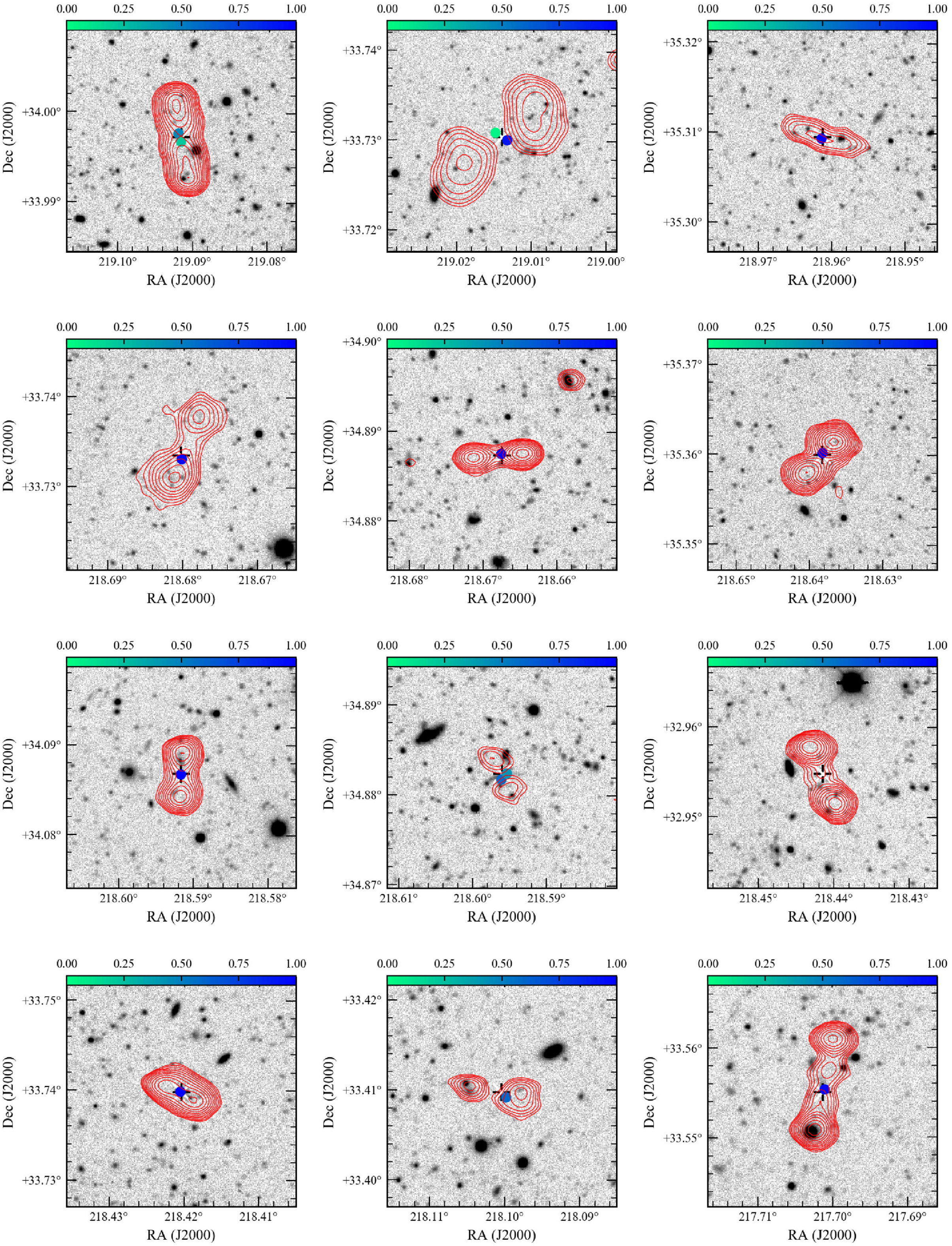

Figure A2. Examples of the radio-optical cross-matches in Class 2. The grey-scale image show the *I*-band NDWFS image. The red contours show the LOFAR 150-MHz image at levels of $3\sigma_{\mathrm{local}} \times [1, 1.4, 2, 2.8, \dots]$, where σ_{local} is the local rms in the LOFAR map at the source position. The blue colour scale shows the LR probability of the matched optical source. Each image is 1.25 arcmin in diameter.

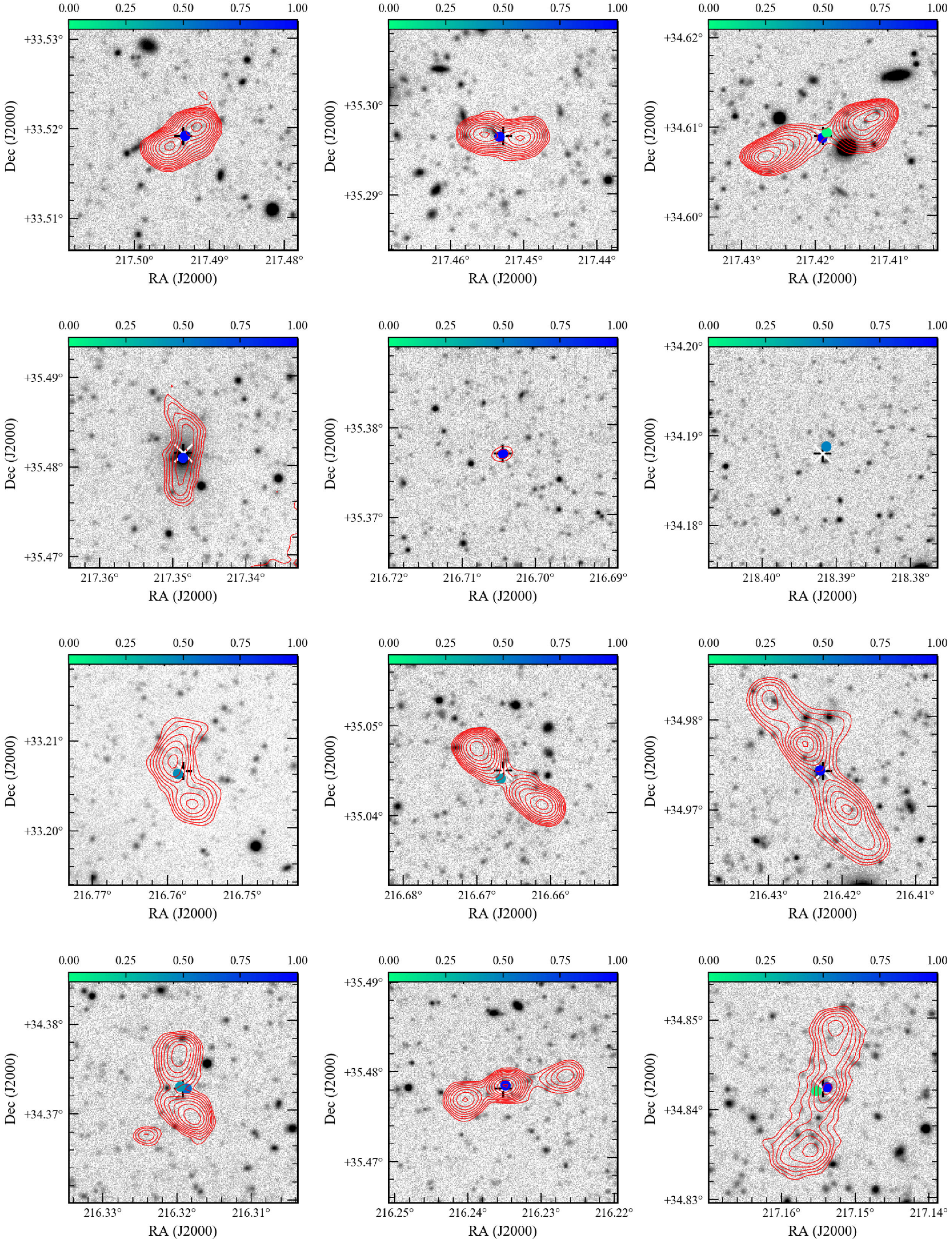

Figure A2 – *continued*

APPENDIX B: EXAMPLE SED FITS

Some examples of the AGNFITTER SEDs, including their components, from each of the three redshift intervals are shown in Figs B1 and B2 for sources with good-quality fits (quantified by likelihood values close to −1) and in Fig. B3 for sources with poor fits (quantified by likelihood values $\lesssim -20$). These include both HERGs and LERGs in each redshift interval.

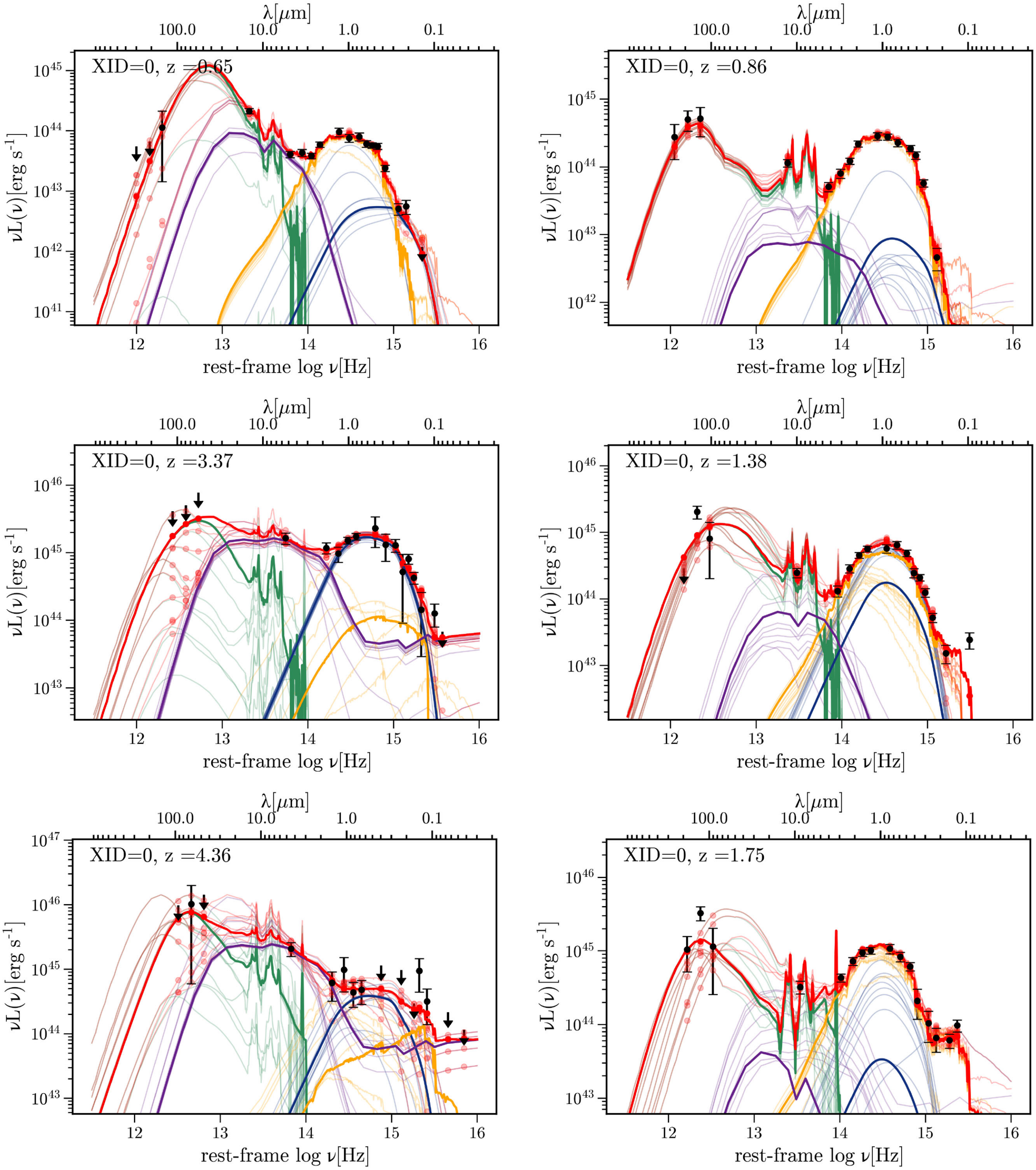

Figure B1. Examples of good-quality SED fits (with likelihood ≈−1) with significant star formation contribution (high $f_{\rm SF}$ values) for HERGs (left) and LERGs (right) in the three redshift bins $0.5 < z \le 1.0$ (top), $1.0 < z \le 1.5$ (middle) and $1.5 < z \le 2.0$ (bottom). In all cases, 10 realizations from the parameters' posterior probability distributions are plotted, giving an indication of the uncertainties in the fitted components. These show the total SED (red) and the individual components: the AGN torus (TO; purple), the starburst (SB; green), the galaxy (GA; yellow), and the blue bump (BB; blue). The red points show the total SEDs integrated across the filter bandpasses and the black points with errorbars show the observed luminosities.

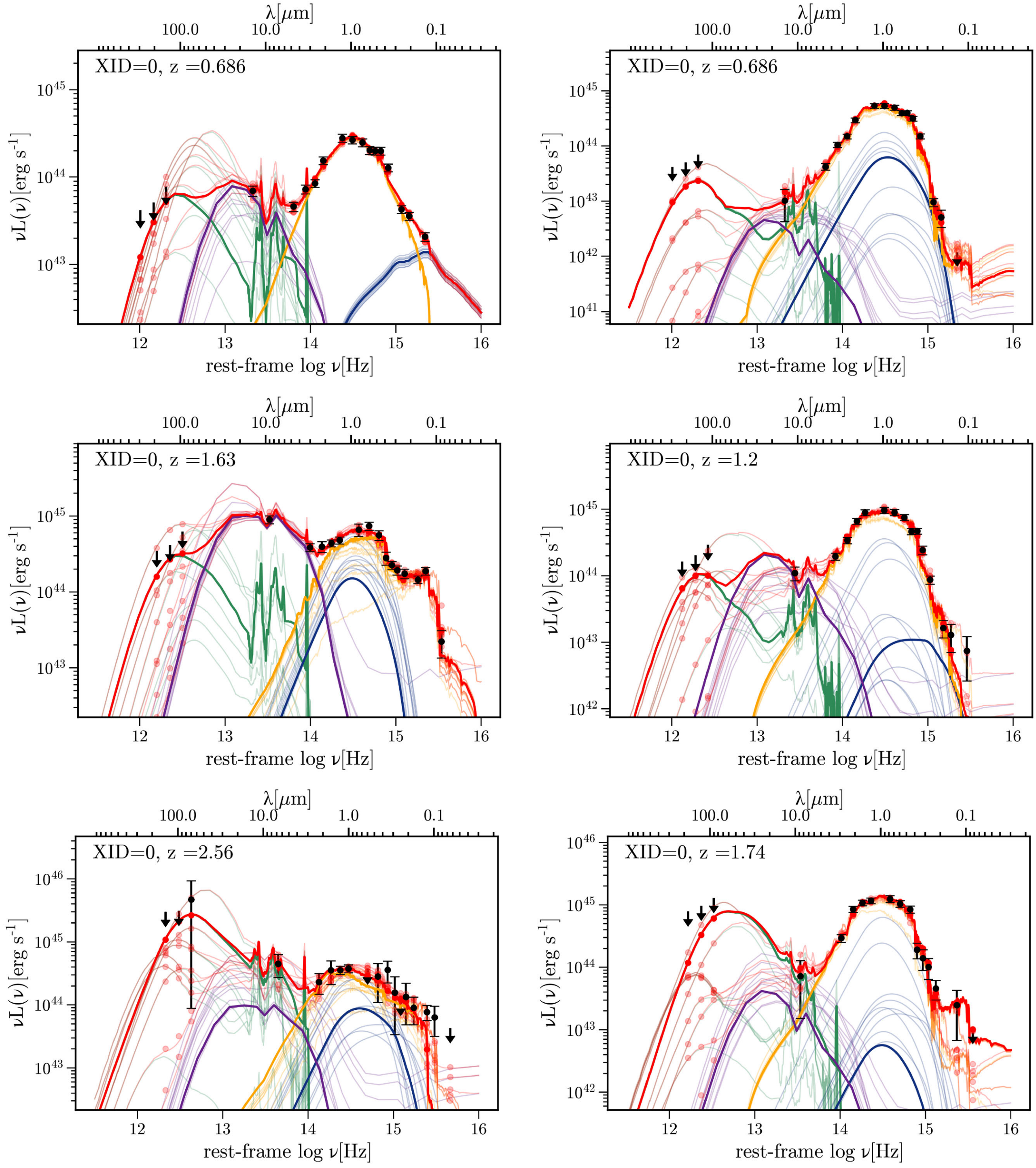

Figure B2. Examples of good-quality SED fits (with likelihood ≈−1) with minimal star formation contribution (low f_{SF} values) for HERGs (left) and LERGs (right) in the three redshift bins $0.5 < z \leq 1.0$ (top), $1.0 < z \leq 1.5$ (middle) and $1.5 < z \leq 2.0$ (bottom). In all cases 10 realizations from the parameters' posterior probability distributions are plotted, giving an indication of the uncertainties in the fitted components. These show the total SED (red) and the individual components: the AGN torus (purple), the starburst (green), the galaxy (yellow) and the blue bump (blue). The red points show the total SEDs integrated across the filter bandpasses, and the black points with errorbars show the observed luminosities.

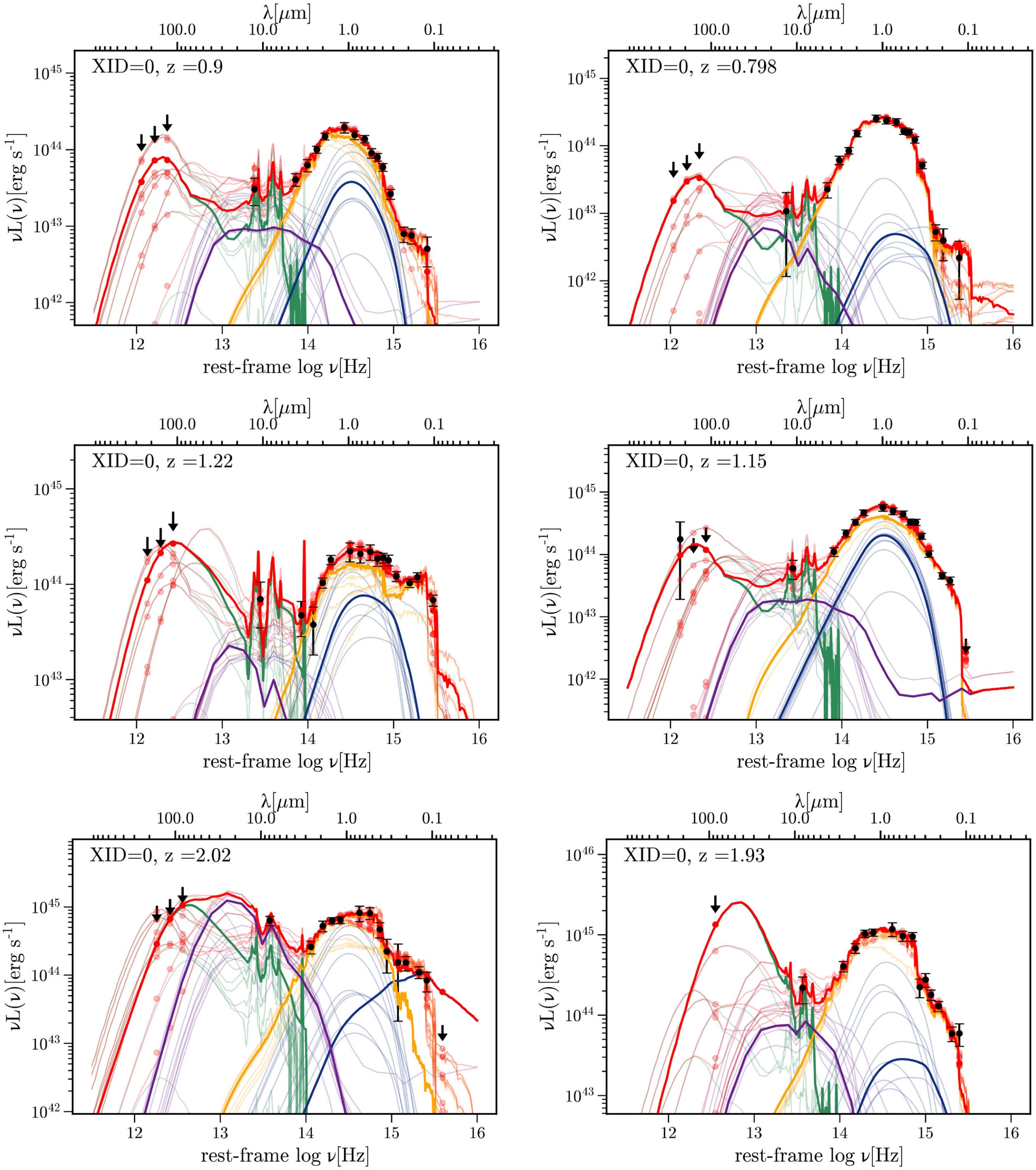

Figure B3. Examples of poorer SED fits (with likelihood ≈−20) for HERGs (left) and LERGs (right) in the three redshift bins $0.5 < z \leq 1.0$ (top), $1.0 < z \leq 1.5$ (middle) and $1.5 < z \leq 2.0$ (bottom). In all cases, 10 realizations from the parameters' posterior probability distributions are plotted giving an indication of the uncertainties in the fitted components. These show the total SED (red) and the individual components: the AGN torus (purple), the starburst (green), the galaxy (yellow), and the blue bump (blue). The red points show the total SEDs integrated across the filter bandpasses, and the black points with errorbars show the observed luminosities.

This paper has been typeset from a TEX/LATEX file prepared by the author.